The Astrophysical Journal, 968:7 (19pp), 2024 June 10 https://doi.org/10.3847/1538-4357/ad434a
© 2024. The Author(s). Published by the American Astronomical Society.
OPEN ACCESS

Observations of Nonthermal Velocities and Comparisons with an Alfvén Wave Turbulence Model in Solar Active Regions

M. Asgari-Targhi[1], D. H. Brooks[2,6], M. Hahn[3], S. Imada[4], E. Tajfirouze[5], and D. W. Savin[3]
[1] Harvard-Smithsonian Center for Astrophysics, 60 Garden Street MS-15, Cambridge, MA 02138, USA
[2] Department of Physics & Astronomy, George Mason University, 4400 University Drive, Fairfax, VA 22030, USA
[3] Columbia Astrophysics Laboratory, Columbia University, 538 West 120th Street, New York, NY 10027, USA
[4] Solar-Terrestrial Environment Laboratory, Nagoya University, Furo-cho, Chikusa-ku, Nagoya, Aichi, 464-8601, Japan
[5] Mathematics, Physics and Electrical Engineering, Northumbria University, Newcastle Upon Tyne NE1 8ST, UK
Received 2024 February 14; revised 2024 April 23; accepted 2024 April 23; published 2024 June 4

Abstract

We present a study of spectral line width measurements from the Extreme-ultraviolet Imaging Spectrometer on Hinode. We used spectral line profiles of Fe XVI 262.984 Å, Fe XIV 264.787 Å, Fe XIV 270.519 Å, Fe XIV 274.203 Å, and Fe XV 284.160 Å, and studied 11 active regions. Previous studies of spectral line widths have shown that in hot loops in the cores of active regions, the observed nonthermal velocities are smaller than predicted from models of reconnection jets in the corona or shock heating associated with Alfvén waves. The observed line widths are also inconsistent with models of chromospheric evaporation due to coronal nanoflares. We show that recent advances in higher resolution Alfvén wave turbulence modeling enables us to obtain nonthermal velocities similar to those measured in active regions. The observed nonthermal velocities for the 11 active regions in our study are in the range of 17–30 km s^{-1}, consistent with the spectral line nonthermal widths predicted from our model of 16 interacting flux tubes, which are in the range of 15–37 km s^{-1}.

Unified Astronomy Thesaurus concepts: Solar physics (1476); Solar coronal heating (1989); The Sun (1693); Solar corona (1483); Solar atmosphere (1477)

1. Introduction

Solar active regions possess closed magnetic field lines that are rooted in the Sun at both ends and are known as coronal loops. Some of these loops have temperatures in the range of 1–3 MK. The physical processes by which these loops are heated are not yet fully understood. However, it is generally assumed that the plasma is heated by dissipation of magnetic disturbances that propagate into the corona from the convection zone below the photosphere. The two main models are nanoflare-heating and wave-heating (e.g., Ionson 1985; Milano et al. 1997; Mandrini et al. 2000). In the nanoflare-heating model, the convective flows below the photosphere are assumed to cause twisting and braiding of the coronal magnetic field lines. The magnetic free energy associated with the braided fields is released in brief reconnection events ("nanoflares") that occur throughout the corona (Parker 1972, 1983, 1988; Cargill & Klimchuk 2004; Patsourakos & Klimchuk 2006, 2009; Imada & Zweibel 2012). In wave-heating models, the convective flows are thought to produce magnetohydrodynamic (MHD) waves such as Alfvén and kink waves that are transverse to the background magnetic field. These waves propagate upward along the magnetic field and dissipate their energy in the corona (Alfvén 1947; Coleman 1968; Uchida & Kaburaki 1974; Wentzel 1974; Hollweg et al. 1982; Heyvaerts & Priest 1983; Antolin & Shibata 2010; Matsumoto & Shibata 2010; McIntosh et al. 2011; van Ballegooijen et al. 2011).

Observations from space- and ground-based telescopes are necessary to test and evaluate these heating models. For example, there is evidence for footpoint motions that can either create twists within the field lines or generate MHD waves. Observational constraints on the amplitudes of the magnetic and velocity perturbations in the corona are essential to understand how the energy is transferred from the lower atmosphere into the corona. Any proposed heating mechanism is expected to provide a self-consistent picture of the chromosphere and corona and to generate sufficient heating of the coronal plasma to the observed temperatures.

The Doppler widths of coronal emission lines provide significant constraints on unresolved plasma flows in the solar atmosphere. The spectral line width mainly consists of three parts, the thermal width, the instrumental width, and the nonthermal width. The thermal line width is usually interpreted under the assumption that the ion temperature is equivalent to the electron temperature. The nonthermal line width is associated with flows caused by turbulence or magnetic reconnection (Hara & Ichimoto 1999; Doschek et al. 2007; Imada et al. 2008). The Extreme-ultraviolet (EUV) Imaging Spectrometer (EIS) on the Hinode satellite has provided information on spectral line broadening for individual coronal loops in active regions (e.g., Young et al. 2007; Tripathi et al. 2009, 2011; Warren et al. 2011). There have also been ground-based observations of spectral line broadening (e.g., Ichimoto et al. 1995; Hara & Ichimoto 1999), and satellite-based measurements from X-ray lines (Acton et al. 1981). The line broadening is generally attributed to MHD waves and/or turbulent flows (Doschek & Feldman 1977; Tian et al. 2011; Doschek 2012), but an alternative interpretation is that the excess broadening is due to ion temperatures being larger than

[6] Present address: Hinode Team, ISAS/JAXA, 3-1-1 Yoshinodai, Chuo-ku, Sagamihara, Kanagawa 252-5210, Japan.

Original content from this work may be used under the terms of the Creative Commons Attribution 4.0 licence. Any further distribution of this work must maintain attribution to the author(s) and the title of the work, journal citation and DOI.

electron temperatures (Billings & Lehman 1962; Knight et al. 1974; Imada et al. 2009).

Alfvén waves have been hypothesized to play a major role in heating the solar corona. To put constraints on the amplitudes of Alfvén waves in an active region observed above the solar limb, Hara & Ichimoto (1999) adopted spectroscopic observations with a coronagraph at the Norikura Solar Observatory (also see Ichimoto et al. 1995). They showed that the nonthermal velocities for Fe X 6374 Å, Fe XIV 5303 Å, and Ca XV 5694 Å have ranges of 14–20, 10–18, and 16–26 km s^{-1}, respectively. They also examined the relationship between the widths of the emission lines and the orientation of the coronal loops relative to the line of sight (LOS). They found that for face-on loops, the nonthermal velocity is approximately constant along the loop; while for edge-on loops, there is a decrease in velocity of about 3–5 km s^{-1} toward the loop top. This decrease in velocity was interpreted as evidence for the existence of Alfvén waves in coronal loops. At the loop top for edge-on loops, the magnetic field is parallel to the LOS, so the transverse waves do not contribute to the LOS velocity.

Based on these observations, Hara & Ichimoto (1999) concluded that Alfvén waves might have velocity amplitudes of 3–5 km s^{-1}. However, we suggest that these values may represent a lower limit on the Alfvén wave amplitude. In observations of face-on loops, Hara & Ichimoto (1999) observed nonthermal velocities in the range of 10–18 km s^{-1}, which represents motions perpendicular to the background field. It seems likely to us that all such perpendicular motions are associated with Alfvénic waves (Asgari-Targhi et al. 2014; van Ballegooijen et al. 2017). These waves could either originate in the photosphere or be produced by reconnection events in the corona. In either case, Alfvén and/or kink waves are the only plausible candidates for producing transverse motions in the corona. Therefore, we suggest that the observations by Hara & Ichimoto (1999) are consistent with Alfvén wave amplitudes in the range 10–18 km s^{-1}.

To place observational constraints on wave-heating theories, we must determine the contribution of the Alfvénic waves to the observed nonthermal velocities. In a series of papers, we have studied the dynamics of Alfvén waves in coronal loops using three-dimensional (3D) reduced MHD models (RMHD; van Ballegooijen et al. 2011; Asgari-Targhi & van Ballegooijen 2012; Asgari-Targhi et al. 2013; van Ballegooijen et al. 2014, 2017). We showed the wave energy flux from the Alfvén wave turbulence is sufficient to heat the coronal loops to a temperature of about 2.5 MK. The Alfvén wave turbulence model also predicts rms velocity amplitudes of the Alfvén waves to be in the range 15–37 km s^{-1} in the corona, with the highest velocities generally occurring near the loop top (Asgari-Targhi et al. 2014).

A key test of this model is to compare the predicted velocities with observations of nonthermal line widths of coronal emission lines. Asgari-Targhi et al. (2014) made such a comparison using EIS data. We compared the observed nonthermal line broadening in Fe XII 192.394 Å for individual coronal loops in a single active region of 2012 September 7 with the LOS velocity from our Alfvén wave turbulence model of the loops. We found that footpoint velocities in the range 0.30–1.50 km s^{-1} can reproduce the observed coronal nonthermal widths of 15–37 km s^{-1}. The footpoint velocities, one of the input parameters of our model are consistent with observed motions of magnetic elements in the photosphere (Abramenko et al. 2011; Chitta et al. 2012). Furthermore, we found that in order to produce the observed nonthermal velocities, we needed to introduce a random flow component parallel to the magnetic field, in addition to the perpendicular velocity due to Alfvén waves.

The analysis of Asgari-Targhi et al. (2014) used the 2″ slit of EIS but assumed an instrumental line width appropriate for a 1″ slit. Therefore, the instrument width was underestimated, which led to an overestimation of the EIS nonthermal velocity. Subsequently, Brooks & Warren (2016) performed a systematic analysis of the instrumental effects that influence EIS spectral line width measurements. Here, we follow their analysis to improve our line width measurements and compare the EIS observations with our Alfvén wave turbulence model.

The objective of this paper is twofold. First, we present a systematic observational study of nonthermal velocity in 11 active regions, only one of which was analyzed in Asgari-Targhi et al. (2014). Second, we use an improved Alfvén wave turbulence model containing multiple flux tubes with high spatial resolution (van Ballegooijen et al. 2017) and compare the simulated nonthermal velocities from our multiple flux tube model with measurements averaged over the whole loop arcade of an active region. This is in contrast to Asgari-Targhi et al. (2014), where the dynamics of flows within individual loops were analyzed using a reduced MHD approximation of a single flux tube and compared with nonthermal velocities derived from EIS observations for individual loops. The emission of the spectral lines we use, from Fe XIV, XV, and XVI, represents an integration along the LOS and therefore potentially contains contributions from both the active region loop arcade and unresolved foreground and background emission. Hahn et al. (2023) have quantified the unresolved component contribution to these lines in an active region, indicating substantial contributions, with an increasing impact as the line formation temperature decreases. This contribution may also be active-region-dependent (Brown et al. 2008). Considering the complexity of the emitting structures, we expect the bright arcade and unresolved (potentially cooler) background to represent multiple loop structures; so these are the appropriate observations to compare with our multiloop model.

The rest of this paper is organized as follows. In Section 2, we discuss the observations and issues involved in measuring nonthermal velocities, including the uncertainties in the instrumental contribution to the line width. In Section 3, we discuss the results from the Alfvén wave turbulence models. Section 4 presents the effects of Alfvén wave turbulence in multiple flux tubes on spectral line broadening. Finally, the discussion and conclusion are given in Section 5.

2. Observations

2.1. Nonthermal Line Widths and Instrumental Width

The observed line width is characterized by its FWHM computed from

$$\mathrm{FWHM} = \left[\left(1.665\frac{\lambda}{c}\right)^2\left(\frac{2k_\mathrm{B}T}{M} + W^2\right) + (\Delta\lambda)^2\right]^{1/2}, \quad (1)$$

where λ is the wavelength, c is the speed of light, k_B is the Boltzmann constant, T is the ion temperature, M is the ion mass, W is the $1/e$ half width of the nonthermal velocity distribution, and $\Delta\lambda$ is the instrumental width. In this formula,

Table 1
Observations of Active Regions

NOAA Number	EIS Data Set	Slit Size
11029	eis_l0_20091026 _035809	1″
11247	eis_l0_20110713_050720	1″
11250	eis_l0_20110715_094619	1″
11082	eis_l0_20100621_142401	2″
11087	eis_l0_20100716_001932	2″
11093	eis_l0_20100810_223844	2″
11108	eis_l0_20100922_112633	2″
11117	eis_l0_20101026_104913	2″
11127	eis_l0_20101123_221756	2″
11135	eis_l0_20101217_155443	2″
11564	eis_l0_20120907_070549	2″

all three components are considered to have Gaussian distributions. The instrumental width profile is crucial for computing the nonthermal width.

For the observational portion of our study, we use the EIS instrument. EIS observes the Sun in two spectral passbands, detecting spectral lines that emanate from a series of ionization states. In specific, it observes the solar corona and upper transition region with high spectral and spatial resolution over 170–210 and 250–290 Å (Korendyke et al. 2006; Culhane et al. 2007). The line centroids and profile widths enable one to measure the motions of plasmas and turbulent or nonthermal line broadenings. In the EIS data, the $\Delta\lambda$ instrumental width is similar in magnitude to W and the thermal broadening. We account for this $\Delta\lambda$ using the calibration tabulated by Young (2011).

2.2. Observational Results

In this study, we considered 11 active regions. The data sets we used are listed in Table 1. The first three were observed with the 1″ resolution slit, and the rest were observed with the 2″ resolution slit. We included data obtained using the two different slit resolutions to determine if the slit resolution has any significant influence on the measurements of the total line broadening. Our analysis did not find any systematic differences. We used spectral line profiles of Fe XVI 262.984 Å, Fe XIV 264.787 Å, Fe XIV 270.519 Å, Fe XIV 274.203 Å, and Fe XV 284.160 Å.

We used the standard routine eis_prep, which is available within the EIS branch of *solarsoft*, to correct for instrumental effects such as the dark current pedestal, and contamination by dusty, warm, and hot pixels (Brooks & Warren 2016). The routine also corrects for the movement of the spectrum on the CCDs due to thermal orbital effects using a neural network model (Kamio et al. 2010). We did not apply the absolute calibration because this has a tendency to increase the line widths. Recent studies highlight the importance of accurate measurements of the instrumental line width, together with detailed assessment of other instrumental characteristics, in deducing the relevant nonthermal velocity (Brooks & Warren 2016; Testa et al. 2016). The method we used is the same as Brooks & Warren (2016). We fit a single Gaussian function to the spectral line profiles of all lines except for Fe XIV 270.520 Å where we also fit the nearby Mg VI 270.394 Å line to improve the line fit. From the fits, we determined the line intensity, Doppler velocity, and line width.

When EIS raster images were missing data, we used images from the Atmospheric Imaging Assembly (AIA; Lemen & Title 2012) for context. AIA is a multilayer telescope on-board Solar Dynamic Observatory (SDO). It provides full disk images of the Sun at high spatial resolution (0.″6 pixels) and high cadence (∼12 s) in the EUV passbands. We used the standard processing (aia_prep routine) to obtain the level-1.0 data (bad pixels removal, despiking, and flat-fielding) from the level-0 data. We converted the pixel image to arcsecond. We extracted regions with EIS dimensions from the full disk images of SDO/AIA. The EIS 1″ slit scans an area of 128″ × 128″ and the 2″ slit rasters over an area of 120″ × 160″.

An example of the Gaussian fits for one of the active regions studied is shown in Figure 1. The line profiles are averages over the whole active region. The results for the other active regions are summarized in the Appendix. The first column in Figure 1 shows the EIS intensity maps for the active region NOAA 11029 observed on 2009 October 26 in two EUV bands, 195.118 Å and 264.860 Å. These channels contain strong lines of Fe XII and Fe XIV and are sensitive to plasma emitted at temperatures $\sim\log T = 6.1$ and 6.3, respectively, where T is measured in units of K. From the line fits, we find that as the wavelength increases from 262.984 Å to 284.160 Å, there is a change in the nonthermal velocity from 21 km s^{-1}, reaching a value of 27 km s^{-1}. This change could be an indication of a temperature effect in these active regions. Alternatively, it could be the result of a wavelength-dependent instrumental effect. The higher value of the nonthermal velocity for Fe XV 284.160 Å, however, could be due to the contamination of this line with Al IX 284.015 Å (Brooks & Warren 2016). The consistency of the values for the two Fe XIV lines suggests that the observed increasing nonthermal velocity might be a temperature dependence. However, we have estimated the uncertainty in the measurements by calculating the standard deviation in nonthermal velocities throughout all the data sets we analyze and find a value of 4.7 km s^{-1} (shown by the dotted lines in the figure). The variation in temperature, therefore, is within the measurement uncertainties.

Figure 2 shows the same active region NOAA 11029 in Fe XII 195.118 Å and Fe XIV 264.787 Å. For the Fe XII 195.118 Å line we removed the contribution of the blended weak line (Fe XII 195.18 Å). Similar EIS maps for the rest of the active regions listed in Table 1 are shown in the Appendix. For the 11 active regions we studied, we find nonthermal velocities in the range of 17–30 km s^{-1}.

3. Alfvén Wave Turbulence Dynamics in Multiple Coronal Loops

We have previously studied the dynamics of Alfvén waves in a single flux tube representing a solar coronal loop in a series of papers using 3D RMHD models (van Ballegooijen et al. 2011, 2014, 2017; Asgari-Targhi & van Ballegooijen 2012; Asgari-Targhi et al. 2013). In these models, the waves are generated by the footpoint motions at the photosphere. The random footpoint motions in our model are created by granule-scale convective flows with velocities of 1.5 km s^{-1} and dynamical timescales of about 1 minute (van Ballegooijen & Asgari-Targhi 2018). The photospheric footpoint motions generate transverse MHD waves that propagate upward along the magnetic field lines. The waves are reflected due to the density variations in the photosphere, chromosphere, and corona creating inward propagating waves. The

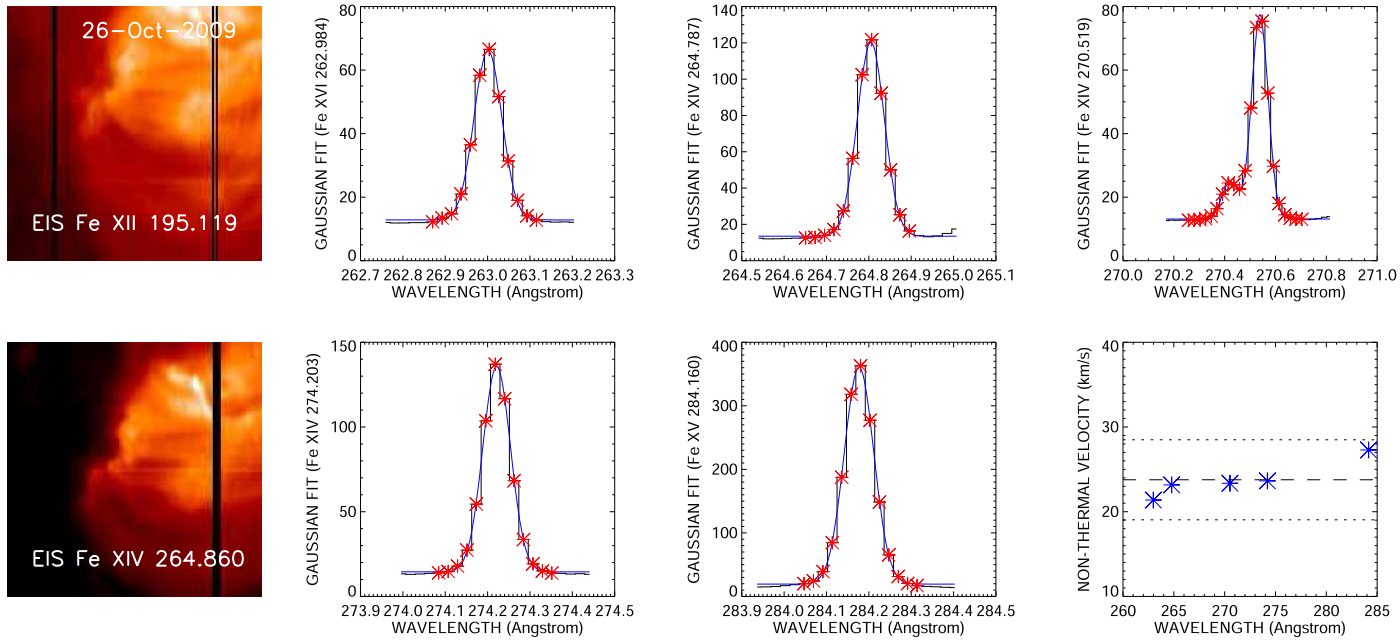

Figure 1. Active region NOAA 11029 observed by EIS with 1″ resolution slit on 2009 October 26 in Fe XII 195.12 Å and Fe XIV 264.860 Å (left column). The next five panels show the Gaussian fits to the spectral lines Fe XVI 262.984 Å, Fe XIV 264.787 Å, Fe XIV 270.519 Å, Fe XIV 274.203 Å, and Fe XV 284.160 Å. The unit for the y-axis is the uncalibrated data number (DN). The histogram and red asterisks show the data and the smooth blue curve shows the fit. The lower right panel shows the nonthermal velocity derived from the Gaussian fits for all the lines (blue asterisks). The dashed line shows the mean for this active region, and the dotted lines show the approximate variation calculated from all the measurements in all the active regions.

counterpropagating waves interact nonlinearly, resulting in turbulence. The energy is dissipated as a result of turbulence, raising the temperature of the corona to 2–3 MK.

Here, we consider a more advanced version of our Alfvén wave turbulence model, consisting of a collection of 16 photospheric flux tubes with square cross sections. This model is the same model that was presented in van Ballegooijen et al. (2017) and is shown in Figure 3. We adopt this model to simulate the emission of the active region loop arcade. Here, we provide a brief review of this model, and in the next section, we compare the nonthermal velocity from this model with observations of active regions listed in Table 1.

Figure 3 shows the discrete flux tubes. The random footpoint motions imposed at the photosphere generate Alfvén waves inside each magnetic field line. The flux tubes expand with height and merge at the height of 520 km in the low chromosphere. The merged field extends from the chromosphere at one end of the loop to the chromosphere at the other end, so the transition regions are located within the merged field (the coronal loop length $L_c = 98.4$ Mm). Note that in Figure 3, the discrete flux tubes are shown and not the merged field lines. We used the RMHD approximation (e.g., Strauss 1976, 1997) to model the waves. The magnetic and velocity perturbations are described by $\delta \boldsymbol{B}_\perp = \nabla h \times \boldsymbol{B}_0$ and $\delta v_\perp = \nabla f \times \hat{s}$, respectively, where $\boldsymbol{B}_0(\boldsymbol{r})$ is the background field, $\hat{\boldsymbol{s}}$ is the unit vector along $\boldsymbol{B}_0$, $h(\boldsymbol{r}, t)$ is the magnetic flux function, and $f(\boldsymbol{r}, t)$ is the velocity stream function.

At the merging height, the waves can travel from the flux tubes into the merged field or vice versa. In the RMHD approximation, the magnetic field strength $B_0(s)$ and plasma density $\rho(s)$ are assumed to be constant over the cross section both for the flux tubes and for the merged field.

The Alfvén waves are described in terms of stream functions $f_\pm(x, y, s, t)$ for the Elsässer variables (Elsasser 1950):

$$z_\pm(x, y, s, t) = \nabla_\perp f_\pm \times \hat{s}, \tag{2}$$

where $\nabla_\perp$ is the perpendicular gradient. The velocity stream function $f = (f_+ + f_-)/2$, and the magnetic flux function $h = (f_- - f_+)/(2v_A)$, where $v_A(s) \equiv B_0/\sqrt{4\pi\rho}$ is the Alfvén speed.

The dynamics of the waves are described by

$$\frac{\partial \omega_\pm}{\partial t} = \mp v_A \frac{\partial \omega_\pm}{\partial s} + \frac{1}{2}\frac{dv_A}{ds}(\omega_+ - \omega_-) + \mathcal{N}_\pm + \tilde{\nu}_\pm \nabla_\perp^2 \omega_\pm, \tag{3}$$

where $\omega_\pm \equiv -\nabla_\perp^2 f_\pm$ are the vorticities of the waves. The four terms on the right-hand side of Equation (3) describe the wave propagation, linear couplings resulting from gradients in Alfvén speed, nonlinear coupling between counterpropagating waves, and wave damping. $\mathcal{N}_\pm$ are nonlinear terms, and $\tilde{\nu}_\pm$ are viscosities. The nonlinear terms are given by

$$\mathcal{N}_\pm = -\frac{1}{2}[\omega_+, f_-] - \frac{1}{2}[\omega_-, f_+] \pm \nabla_\perp^2\left(\frac{1}{2}[f_+, f_-]\right) \tag{4}$$

where $[\cdots, \cdots]$ is the bracket operator:

$$[a, b] \equiv \frac{\partial a}{\partial x}\frac{\partial b}{\partial y} - \frac{\partial a}{\partial y}\frac{\partial b}{\partial x}, \tag{5}$$

with $a(x, y)$ and $b(x, y)$ being two arbitrary functions. The Fourier analysis is used to describe the dependence of the waves on the x and y coordinates, and finite differences in the s direction along the loop. The dynamics of the waves are simulated for a period of 3000 s during which the Alfvén wave

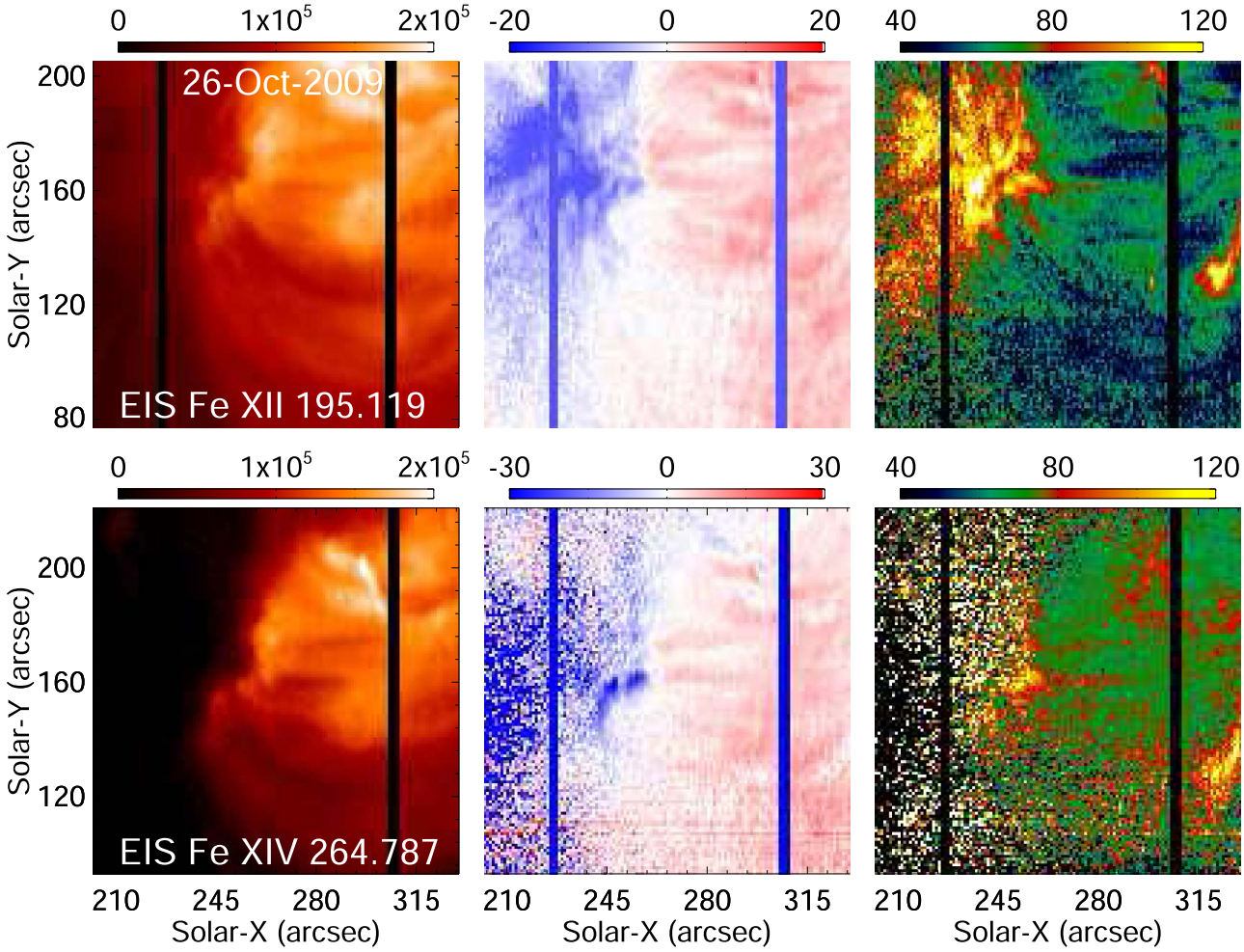

Figure 2. Imaging spectra of intensity in units of ergs cm^{-2} s^{-1} sr^{-1}, Doppler velocity in units of km s^{-1}, and nonthermal velocity (FWHM) in units of km s^{-1} for the active region NOAA 11029 in Fe XII 195.12 Å (top row) and Fe XIV 264.787 Å (bottom row).

turbulence is generated along the field lines, depositing energy and heating the corona.

4. Effects of Alfvén Waves on Spectral Line Broadening

In this section, we simulate the effects of the Alfvén waves on the Doppler shift and Doppler width for the modeled field lines and compare those quantities with the observations of nonthermal velocity presented in Section 2.2 and the Appendix.

In order to compare the current model with observations, we simulate the impact of the modeled waves on the Doppler shift and Doppler width of an observed spectral line, assuming a lateral view of the coronal loop (toward the $+y$ direction). Subsequently, the LOS velocity is represented by v_y, and the observed Doppler shift is directly proportional to the mean value of v_y along the LOS, denoted as $\langle v_y \rangle$. Additionally, the nonthermal component of the Doppler width scales with the velocity variance σ_y, expressed as $\sigma_y^2 = \langle v_y^2 \rangle - (\langle v_y \rangle)^2$. We simplify by assuming constant emissivity and thermal width of the spectral line across the loop cross section. Consequently, $\langle v_y \rangle$ and $\langle v_y^2 \rangle$ are approximated as simple averages over the y coordinate in our numerical model. To accommodate instrumental effects, we also average in the x-direction over a distance $\Delta x = D_0 \Delta\theta$, where $\Delta\theta$ represents the angular resolution of the instrument, and D_0 denotes the Sun–Earth distance.

Figure 4 shows the Doppler velocities at time $t = 1873.5$ s in the simulation. The three columns show maps of intensity (INT), average LOS velocity (VLOS), and average nonthermal velocity (VNTH). The top row shows the maps from our RMHD model based on Alfvén wave turbulence. The second row shows maps for an instrument with a spatial resolution of 290 km, such as the Multi-slit Solar Explorer (MUSE; De Pontieu et al. 2021) and pixel size of 121 km, when projected onto the Sun. Brooks et al. (2013) found this resolution to be sufficient to resolve coronal loops. The bottom row represents the EIS instrument with a spatial resolution of about 1450 km (2″) and pixel size of 725 km (1″). In all panels of Figure 4, we only show the merged field and ignore the field curvature so each image is the loop projected on the (s, x) plane. The width of the image $w(s)$ varies with position s along the loop, but the vertical size of each image corresponds to a width of 10 Mm along the entire length of the loop. We have just expanded the vertical scale relative to the horizontal scale to show the velocity structures inside the loop more clearly. The first column of Figure 4 shows the intensity using an inverted grayscale. As the color bar indicates, black signifies higher intensity. At full resolution, the boundaries of the observed structure appear sharp due to the assumption of a square cross section for the loop, and the emissivity is presumed to diminish beyond the simulation domain. However, at lower resolutions, the edges become less defined, and the pixel size

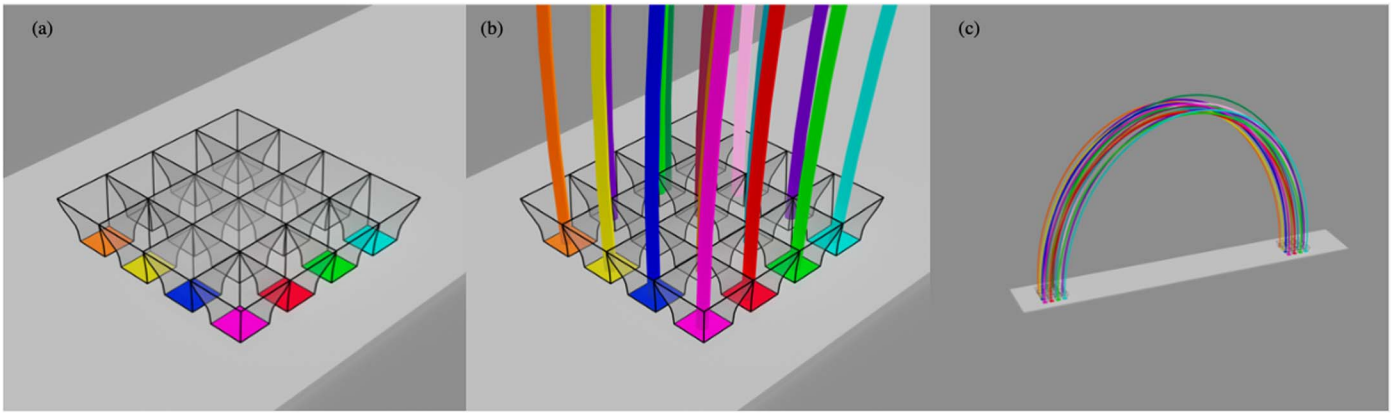

Figure 3. (a) An array of 4×4 flux tubes merging into a space-filling field. (b) Close-up of the left footpoint. The colored squares indicate the intersections of the flux tubes with the plane $z = 0$. (c) Magnetic field lines heated by Alfvén wave turbulence (AWT). The colors of the field lines are randomly selected.

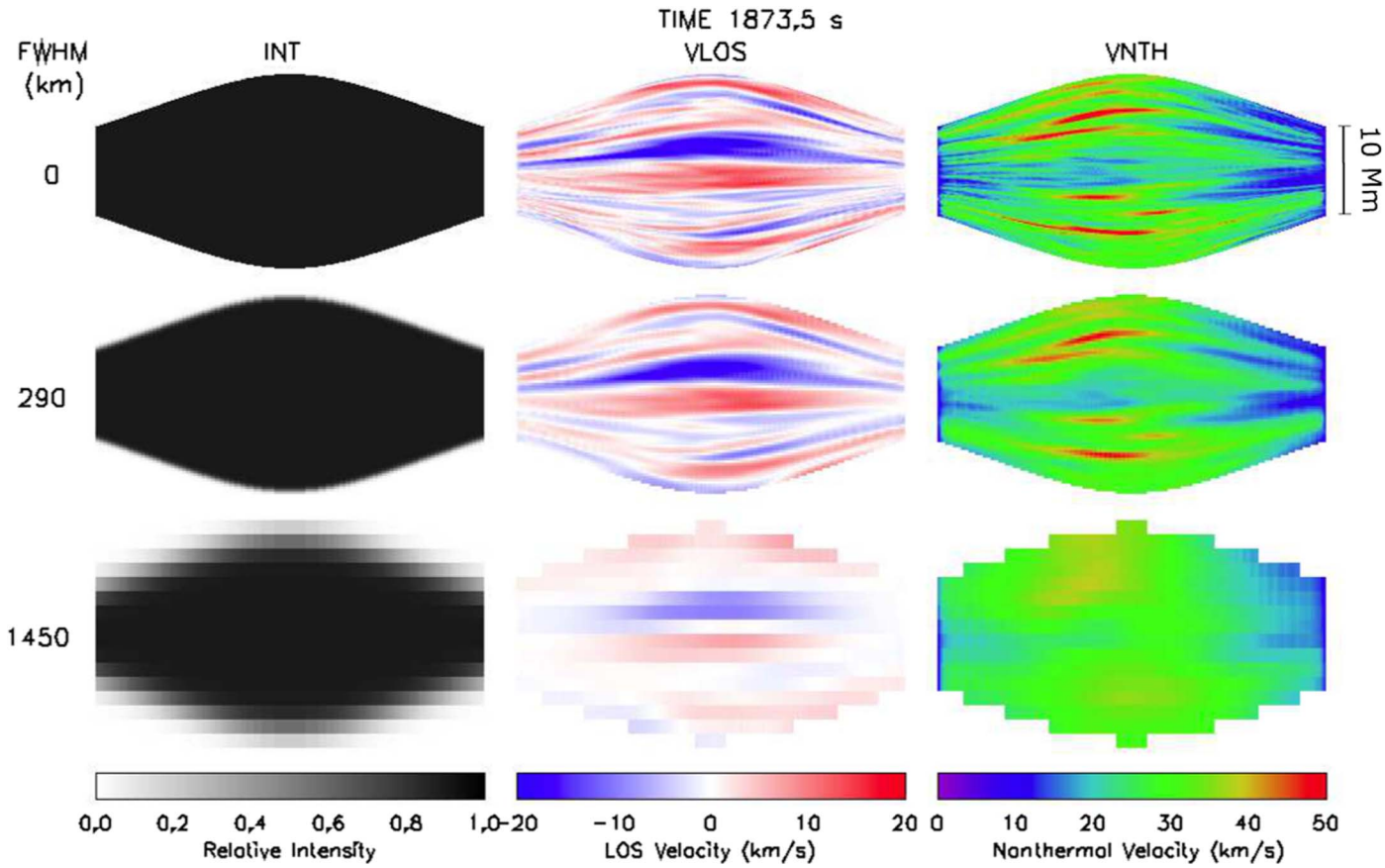

Figure 4. Effect of the modeled waves on the Doppler shift and Doppler width of a spectral line, assuming the merged field lines are viewed from the side. The time in the model is 1873.5 s. The three columns show the intensity (INT), LOS velocity (VLOS), and nonthermal velocity (VNTH). The three rows correspond to different values of the spatial resolution of our model, MUSE, and EIS ($\Delta x = 0$, 290 and 1450 km, respectively). The field curvatures are neglected, so the loop axes run horizontally through the middle of each image. The transverse (vertical) scale is greatly expanded compared to the longitudinal scale. Spatial smearing and pixelation have been applied to the data. The velocity amplitudes are indicated by the color bars.

becomes more apparent. This figure is similar to Figure 4 presented in van Ballegooijen et al. (2017), except that those authors looked at these maps at a different time in their simulation.

The middle column shows the predicted VLOS as a color-scale image. The velocity scale is given at the bottom of the column. The upper panel shows the simulated velocity map from our model. Note that VLOS varies rapidly in the x-direction (vertical) while showing gradual changes in the s-direction (horizontal), suggesting that the internal motions exhibit coherence along the loop. The changes in the VLOS appear on a length scale of about 500 km. The rms value of VLOS over the entire image is $5.8\,\mathrm{km\,s^{-1}}$. The VLOS in the middle panel is shown for an instrument such as MUSE. The velocity pattern from this instrument is almost identical to the velocities from our model in the top panel. The rms velocity from this instrument is $5.1\,\mathrm{km\,s^{-1}}$, suggesting such instruments would resolve well the velocity variations from our model.

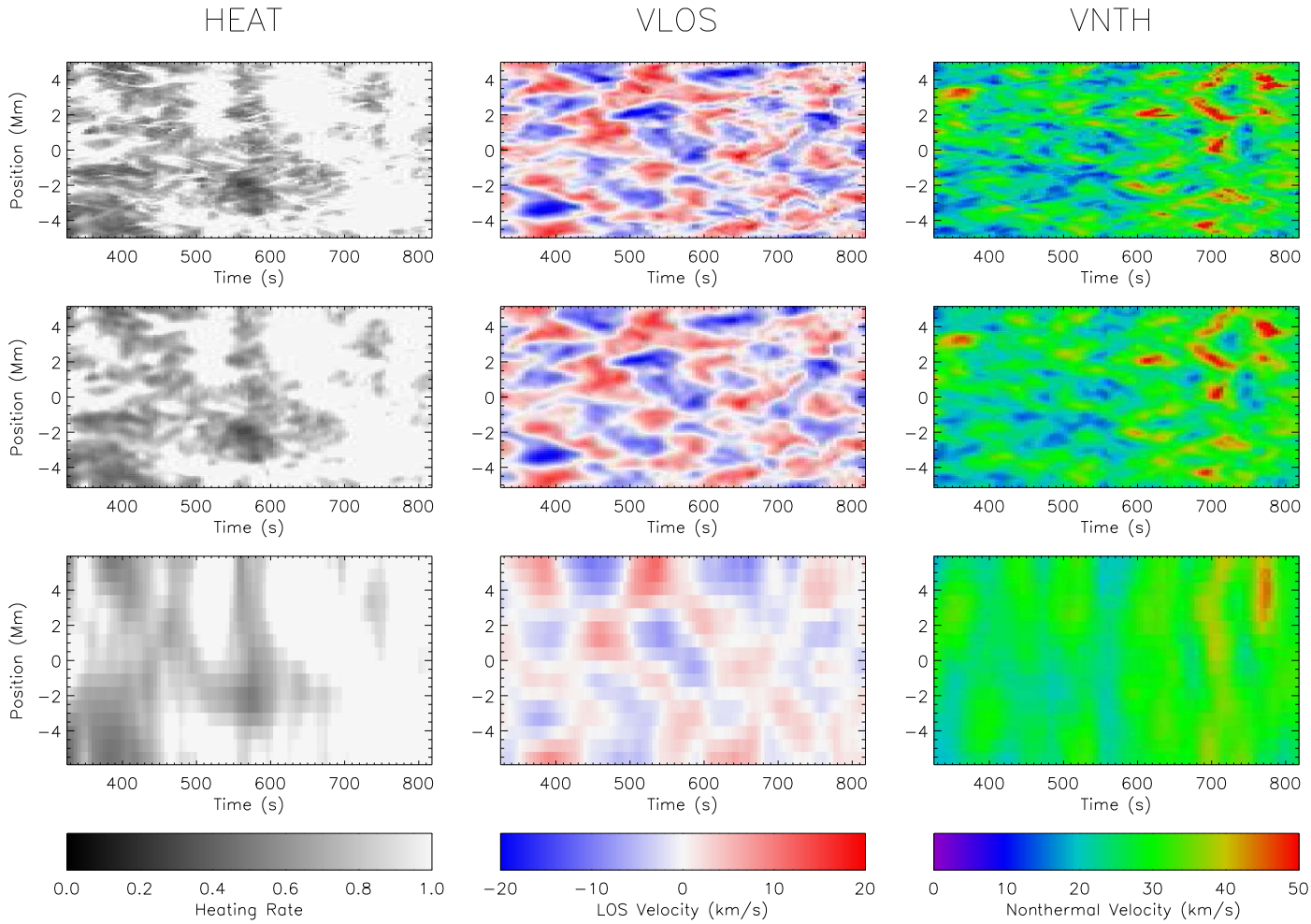

Figure 5. Time slices of heating rate (HEAT), LOS velocity (VLOS), and nonthermal velocity (VNTH) at a spatial resolution of our RMHD model (top row), a MUSE-like instrument at 290 km (middle row), and EIS at 1450 km (bottom row).

The bottom VLOS panel shows the velocity fluctuations with an rms value of 2.7 km s^{-1} from an instrument with a spatial resolution of EIS. The uncertainty in EIS velocity measurements is on the order of 4.5 km s^{-1} (Kamio et al. 2010), though higher sensitivity can be inferred from time-series spectra (Mariska & Muglach 2010). Still, detecting the VLOS fluctuations simulated here would be challenging with EIS.

The right column of Figure 4 shows the predicted VNTH from our model, a MUSE-like instrument, and the EIS instrument. The corresponding velocity scale is given at the bottom of this column. The value of VNTH averaged over the image from the transverse waves in our model is about 27 km s^{-1}. This is consistent with the spectroscopic observations of nonthermal velocities from EIS shown in the bottom right panels of Figures 1, 2, and A1–A20. These velocities have a range of ∼17–30 km s^{-1}.

Figure 5 shows the time–position plot across the 10 Mm width at the top of the loop. The first column shows the heating rate integrated along the LOS, the second column the VLOS, and the third column VNTH. The first row is the Alfvén wave turbulence model, the second row is the MUSE-like instrument, and the third is the EIS instrument. The nonthermal velocity map from our model shows a variation of ∼15–37 km s^{-1}, in agreement with the VNTH from the analyzed EIS observations (Figures 1, 2, and A1–A20) and in accordance with the values shown in the first panel of Figure 4. The brightenings in the heating rate map from our model (top panel) are indicators of the large heating rates.

5. Discussion and Conclusion

In this paper, we presented a review of nonthermal velocity and instrumental width measurements. We then analyzed the EIS observations of spectral line broadening in Fe XVI 262.984 Å, Fe XIV 264.787 Å, Fe XIV 270.519 Å, Fe XIV 274.203 Å, and Fe XV 284.160 Å, and studied 11 active regions observed with 1″ and 2″ resolution slits. We found that the nonthermal velocities fall in the range of 17–30 km s^{-1}, with an uncertainty of 4.7 km s^{-1}. We also noticed a possible tendency for the nonthermal velocity to increase with wavelength and/or temperature, although the change is close to the measurement uncertainty. The nonthermal velocity measurements from the observations were compared with our Alfvén wave turbulence model built of multiple flux tubes.

Imada et al. (2009) analyzed ion thermal temperatures in an active region observed by EIS using the spectral lines Fe XVI 262.98 Å and S XIII 256.69 Å. They found that the typical nonthermal velocities were 13 km s^{-1} at temperatures of ∼2.5 MK. The highest nonthermal velocities (>20 km s^{-1}) were observed between the bright points in Fe XVI. Testa et al. (2016)

analyzed spectroscopic observations of the Fe XII emission line at 1349.4 Å using the Interface Region Imaging Spectrograph (IRIS; De Pontieu et al. 2014) and at 195.119 Å using EIS observations. IRIS has a high spatial resolution of 0.″33 and observes the chromosphere and transition region, creating slit-jaw images and high-resolution spectra. In their study of the spectral properties of Fe XII, Testa et al. (2016) considered two active region data sets where the spectral properties were determined by fitting the spectra with one Gaussian in the case of IRIS observation and two Gaussians in the case of EIS observations. The instrumental width in their calculation for IRIS was estimated to be of the order of 4 km s^{-1} (De Pontieu et al. 2014), while for EIS it was of the order of 61–75 km s^{-1}. The nonthermal width measured from IRIS data sets was 10–15 km s^{-1} for active region moss, while it peaked at ∼20 km s^{-1} from EIS observations. Brooks & Warren (2016) found that the absolute calibration of the EIS data could potentially increase the line width, and this was confirmed by Testa et al. (2016). Both Testa et al. (2016) and Brooks & Warren (2016) suggest that the nonthermal velocity does not increase with temperature.

Note, however, that differing assumptions and observational targets make direct comparisons of our results with previous work difficult. Our measurements focus on the nonthermal velocities of whole active regions, whereas Imada et al. (2009) studied the spatial variation of nonthermal velocities within an active region. They also assumed that Fe XVI 262.98 Å and S XIII 256.69 Å have the same ion temperature and nonthermal velocity, whereas we assume the lines are formed at the temperature of the peak of the ionization fraction, which is slightly higher for Fe XVI 262.98 Å. Testa et al. (2016) made measurements in the moss at the footpoints of high-temperature loops, and Brooks & Warren (2016) studied isolated portions of the high-temperature loop tops. It is possible that nonthermal velocities behave differently with temperature in different specific features of an active region, and this needs further investigation.

In our study, we analyzed the average nonthermal velocity for 11 active regions and found it to be in the range of 17–30 km s^{-1}. We compared these observations with the Alfvén wave turbulence model of 16 interacting field lines. The Doppler shift and Doppler width of the simulated waves in these loops presented in Figure 4 show that the rms value of VLOS over the entire velocity map is 5.8 km s^{-1}. This VLOS rms could be resolved by an instrument such as MUSE (De Pontieu et al. 2021) with its high spatial resolution of 290 km. This confirms that these velocity variations would be well resolved in such observations. The simulated nonthermal velocity from Figure 5 showed these velocities to have a range of 15–37 km s^{-1}, consistent with the nonthermal velocities from the EIS observations.

Acknowledgments

M.A.-T., M.H., and D.W.S. are supported by the NASA Heliophysics Guest Investigator program grant 80NSSC20K0692 to the Smithsonian Astrophysical Observatory (SAO) and Columbia University. The work of D.H.B. was performed under contract to the Naval Research Laboratory and was funded by the NASA Hinode program.

Appendix
Observational Results: Gaussian Analysis

A.1. Active Regions Observed with 1″ Slit

Figures A1–A4 show our results using the 1″ slit. These results are in good agreement with those from the 2″ slit. We estimated the intensity, Doppler velocity, and line width by a single Gaussian fitting. We used the eis_auto_fit routine to fit a Gaussian to the spectrum. All the dark stripes seen in the images were set to the missing values in the data window structure and they are ignored by the fitting routine. We used eis_get_fitdata to extract the line quantities from the output structure of the eis_auto_fit.

Figures A1 and A3 show the EIS intensity, velocity, and line width for the active regions 11247 and 11250 from Table 1 observed with 1″ slit. The first column in Figures A2 and A4 shows intensity maps from EIS or AIA. The other panels show the Gaussian fit to the spectral lines for Fe XVI 262.984 Å, Fe XIV 264.787 Å, Fe XIV 270.519 Å, Fe XIV 274.203 Å, and Fe XV 284.160 Å. The last panel in the figures plots the FWHM as a function of wavelength. The line profiles are averages over the whole active region.

Figure A2 presents the active region 11247 observed on 2011 July 13. The nonthermal velocity is 18 km s^{-1} for Fe XVI 262.984 Å and has a steady increase to 31 km s^{-1} for Fe XV 284.160 Å. The nonthermal line broadening is similar for Fe XIV 270.519 Å and Fe XIV 274.203 Å.

Figure A4 shows the active region 11250 observed on 2011 July 15. The nonthermal velocity for this region has the same trend as the active regions shown in Figures 1, A2, A6, A14, A16, and A20. In all these regions, the velocity increases between the wavelengths 262.984 Å and 284.160 Å, reaching its highest value at 284.160 Å.

A.2. Observations with 2″ Slit

Our results for the 2″ slit are shown in Figures A5–A20. Figures A5, A7, A9, A11, A13, A15, A17, and A19 show the intensity, velocity, and line width for active regions observed by the 2″ slit. The first column in Figures A6, A8, A10, A12, A14, A16, A18, and A20 shows context intensity maps from EIS or AIA. Columns 2, 3, and 4 show the Gaussian fit to the spectral lines for Fe XVI 262.984 Å, Fe XIV 264.787 Å, Fe XIV 270.519 Å, Fe XIV 274.203 Å, and Fe XV 284.160 Å, except for Figure A20, which does not have the plot for Fe XIV 270.519 Å due to lack of proper observation in this line for 2012 September 7.

Figure A8 shows the active region 11087 observed on 2010 July 16. The first panel shows the AIA intensity maps in 193 Å and 211 Å. The nonthermal line broadening increases between 262.984 Å and 264.787 Å. It decreases at 270.519 Å, and increases again, reaching a maximum at 284.160 Å. The active regions shown in Figures A10, A12, and A18 have the same trend.

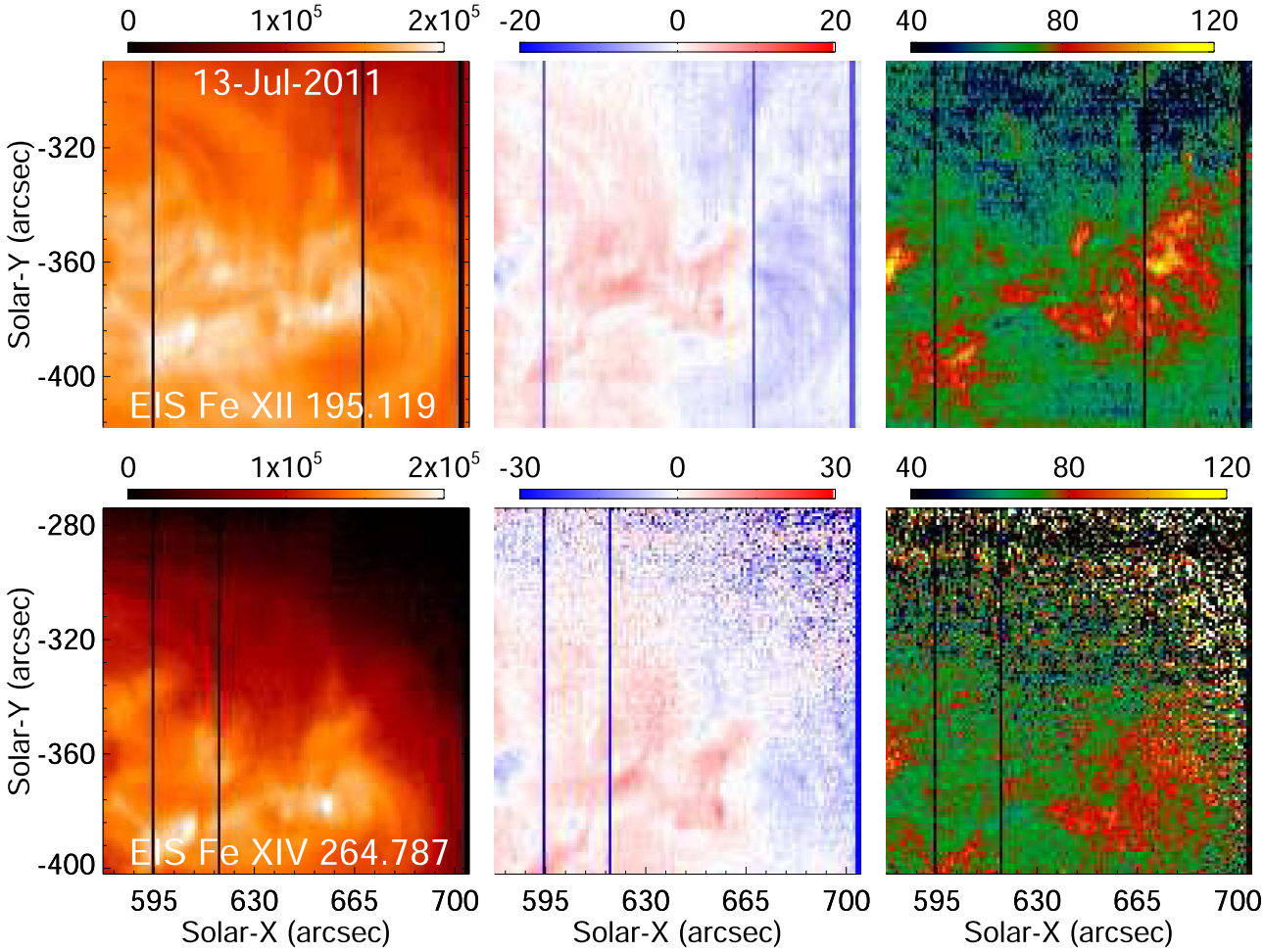

Figure A1. Same as Figure 2 but for the active region NOAA 11247 observed on 2011 July 13.

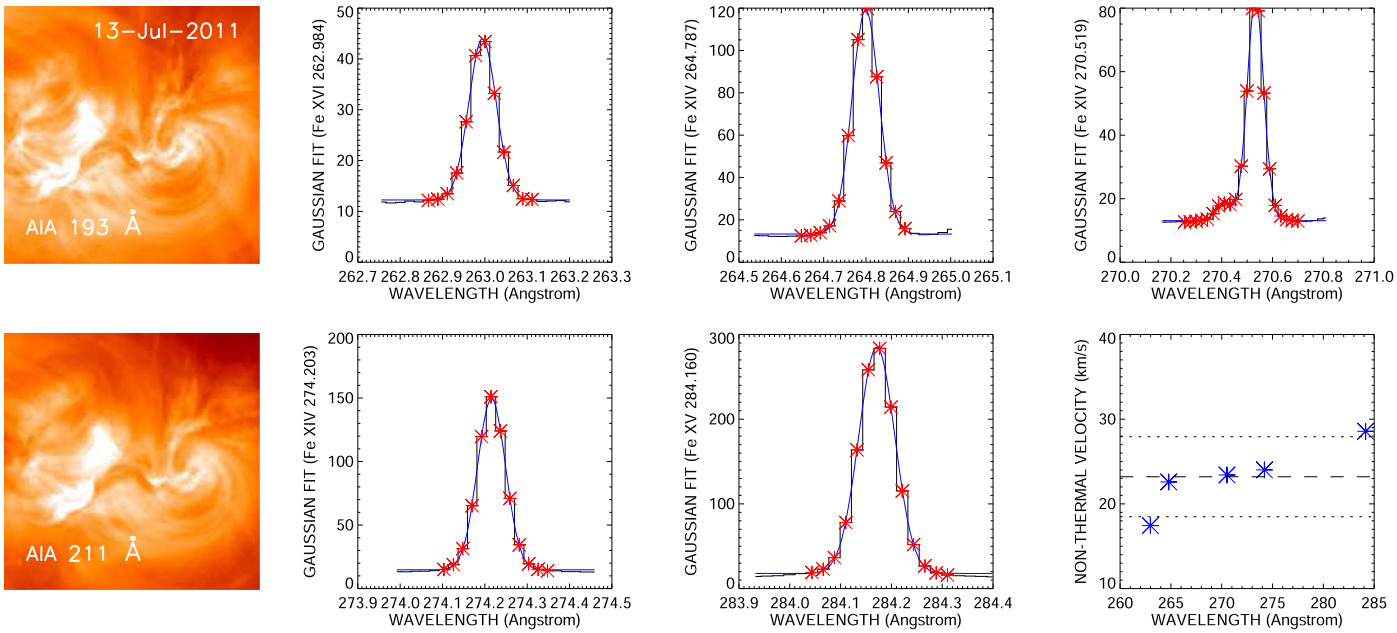

Figure A2. Same as Figure 1 but for the active region NOAA 11247 observed on 2011 July 13.

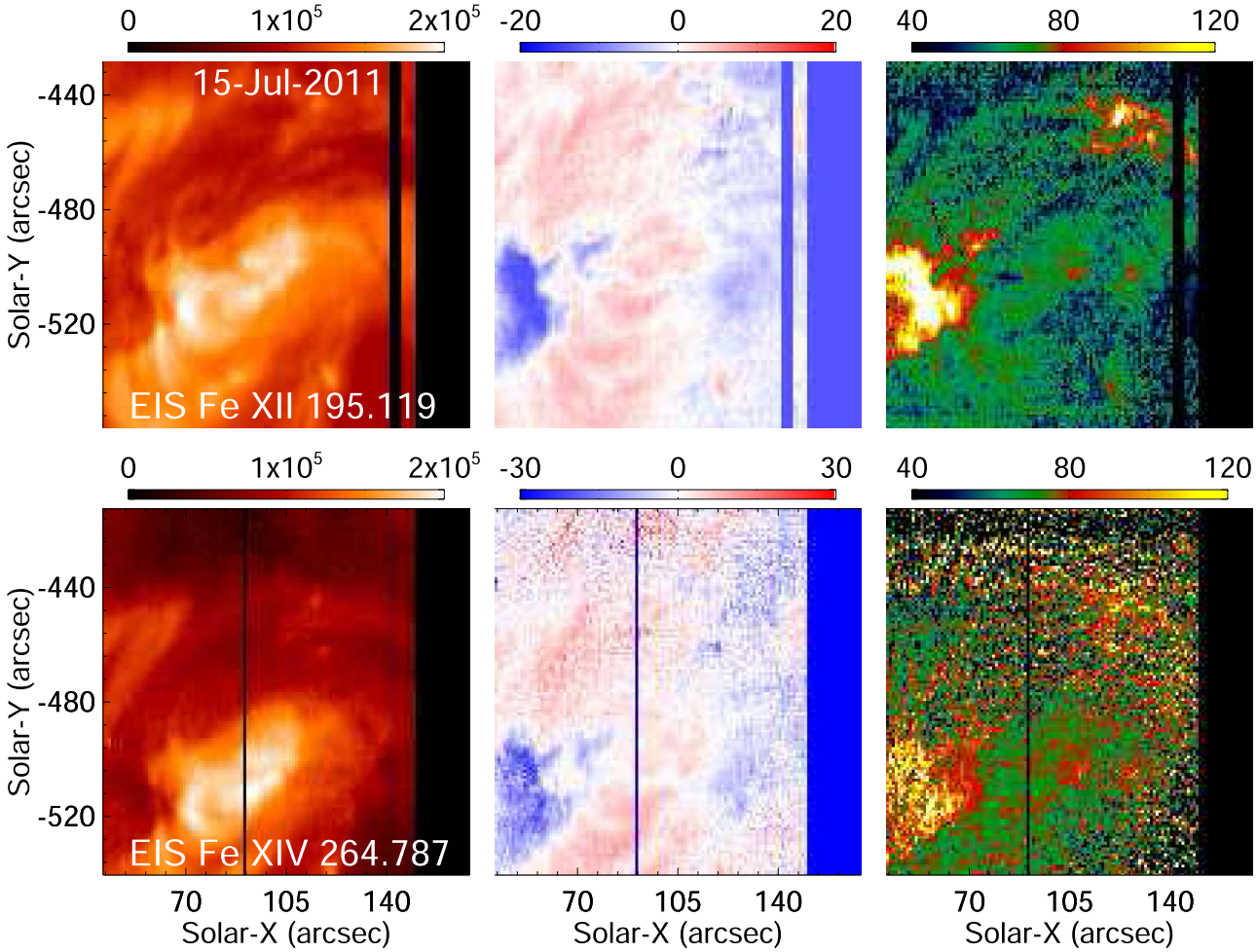

Figure A3. Same as Figure 2 but for the active region NOAA 11250 observed on 2011 July 15.

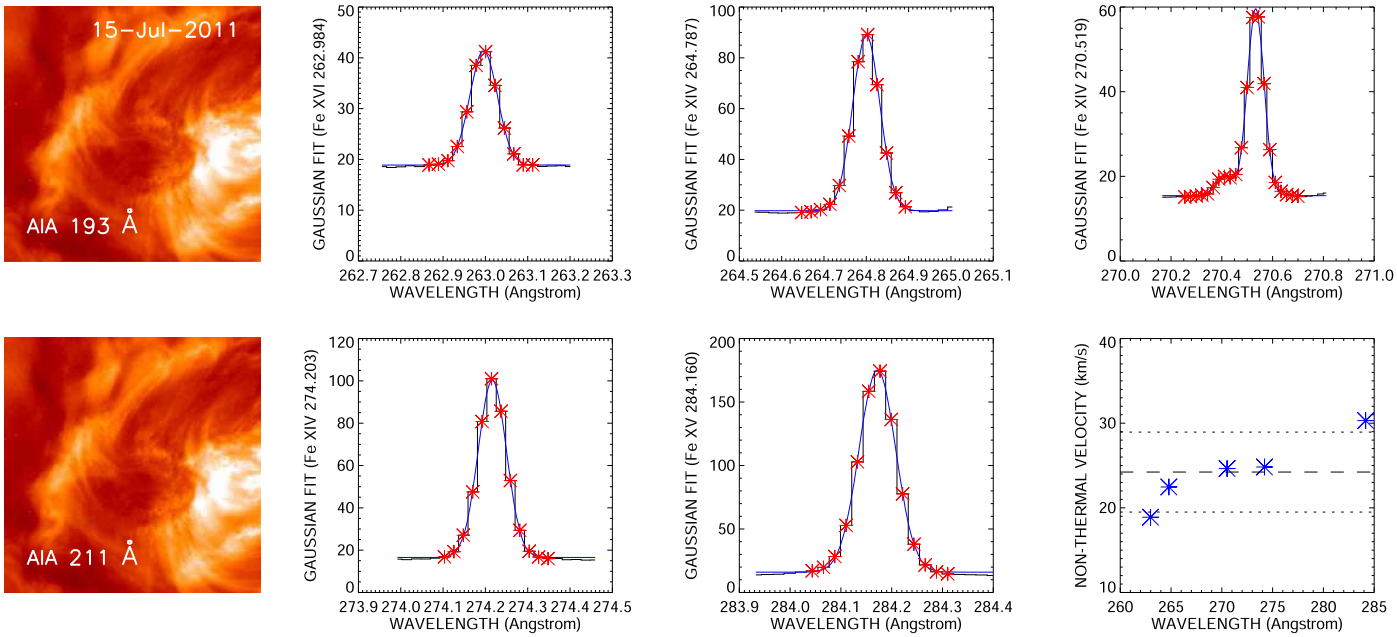

Figure A4. Same as Figure 1 but for the active region NOAA 11250 observed on 2011 July 15.

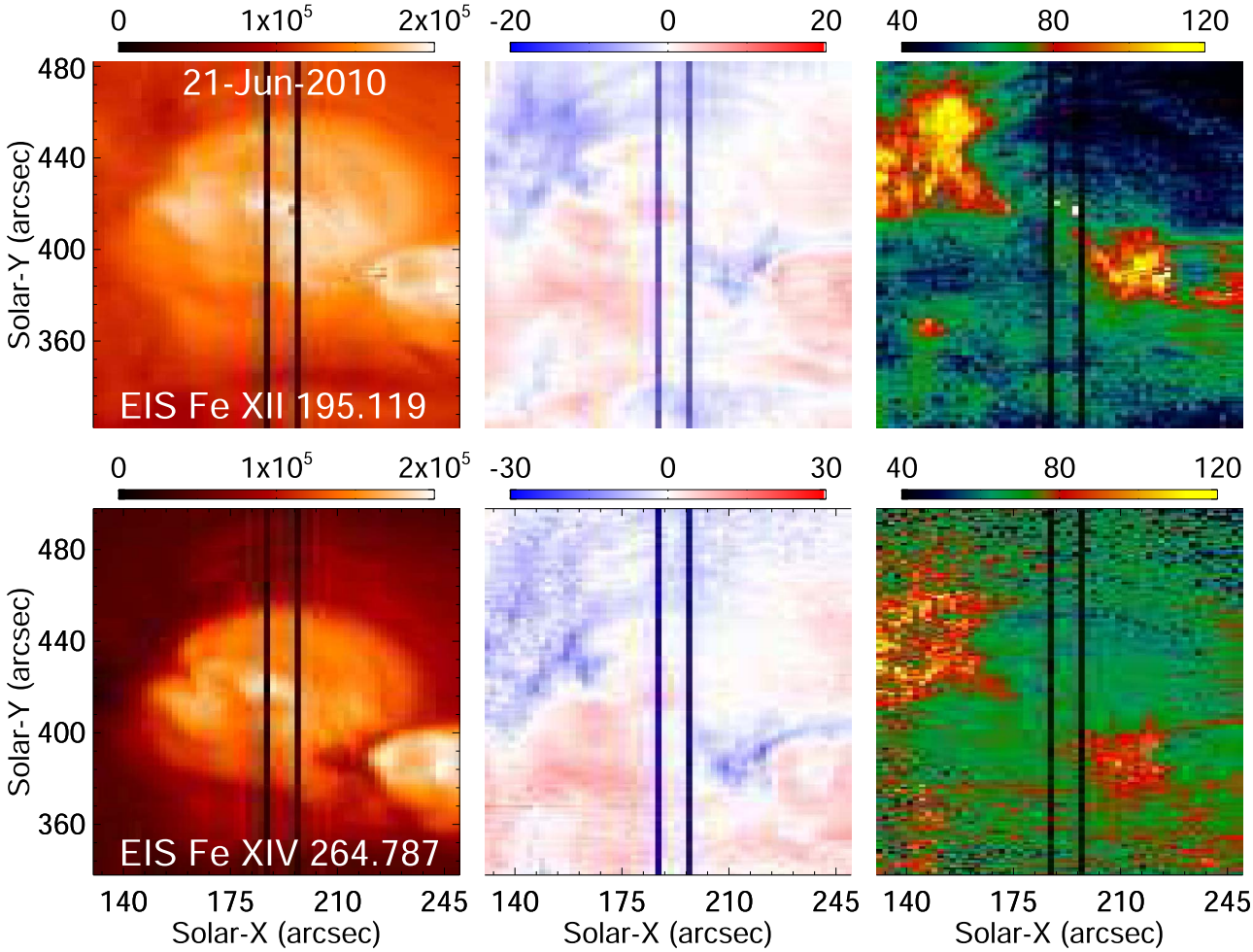

Figure A5. Same as Figure 2 but for the active region NOAA 11082 observed on 2010 June 21.

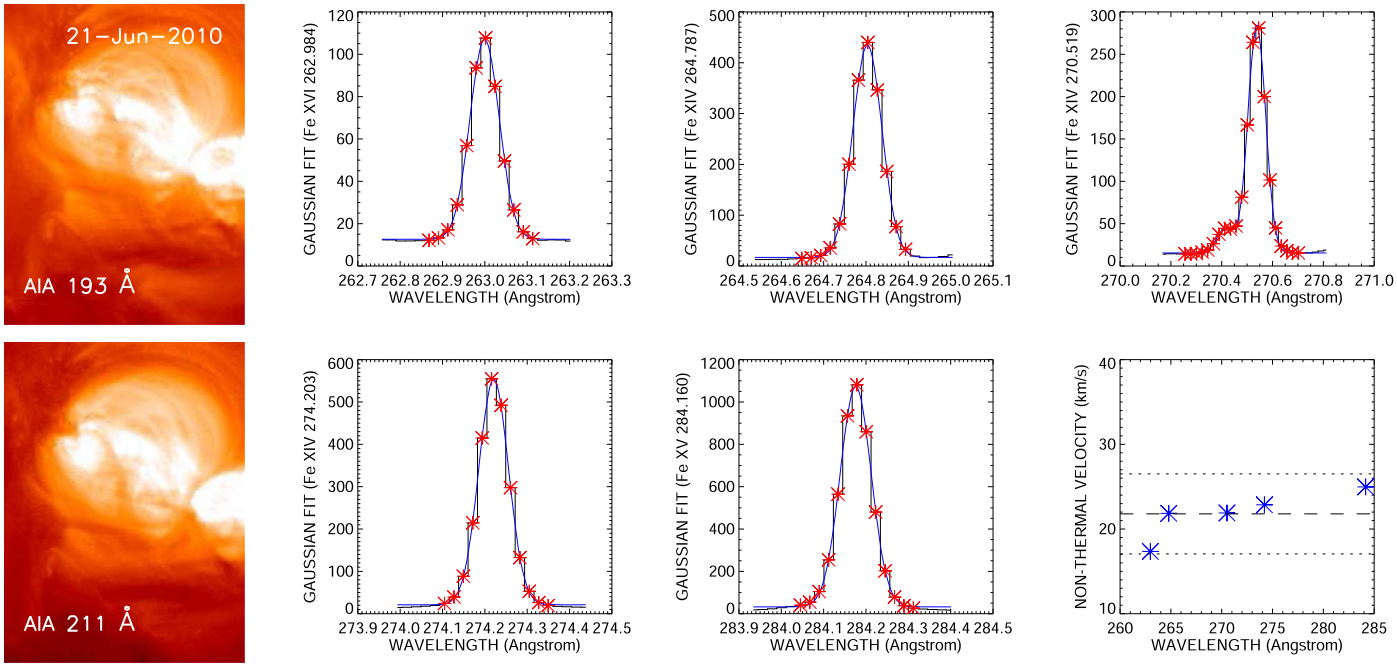

Figure A6. Same as Figure 1 but for the active region NOAA 11082 observed on 2010 June 21.

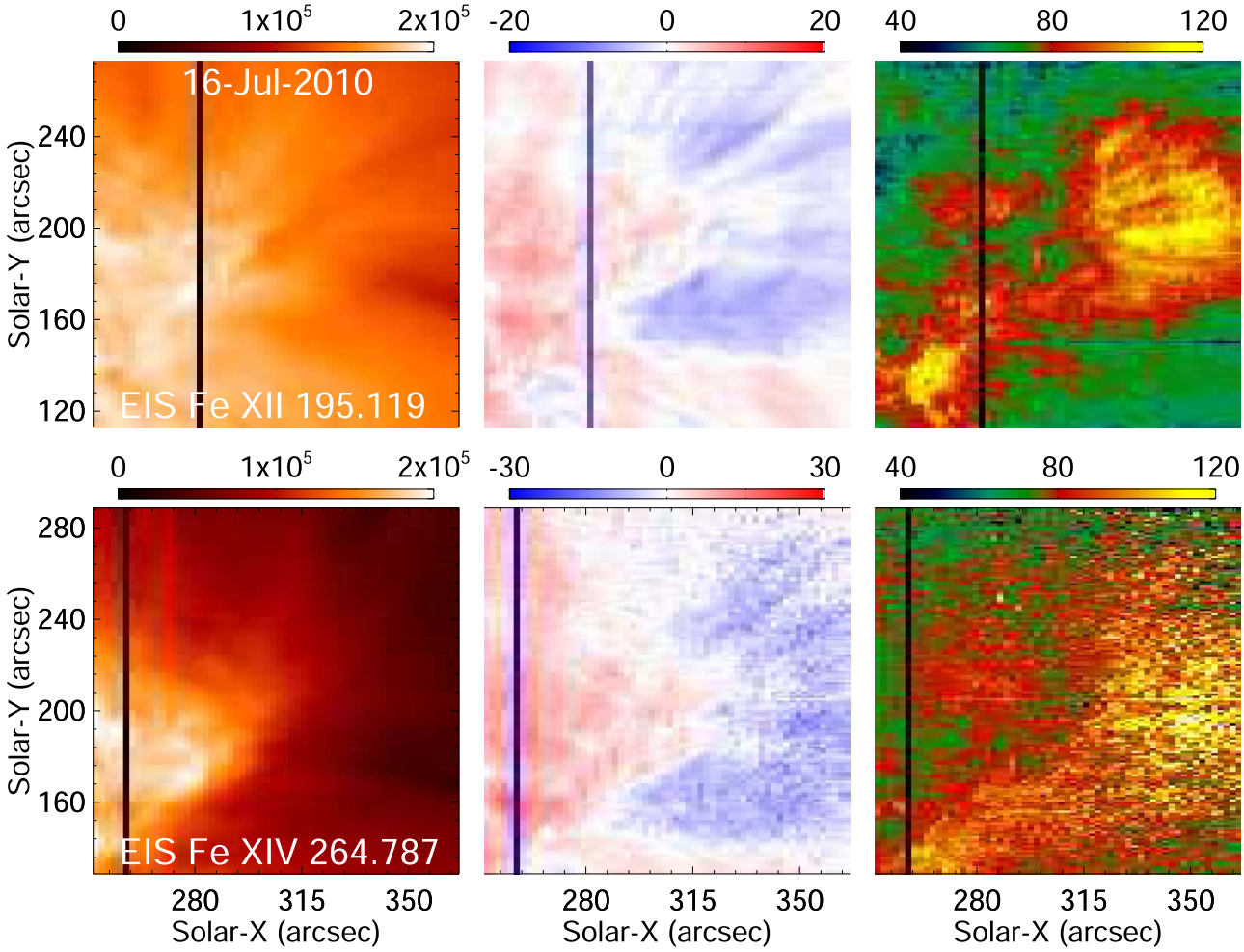

Figure A7. Same as Figure 2 but for the active region NOAA 11087 observed on 2010 July 16.

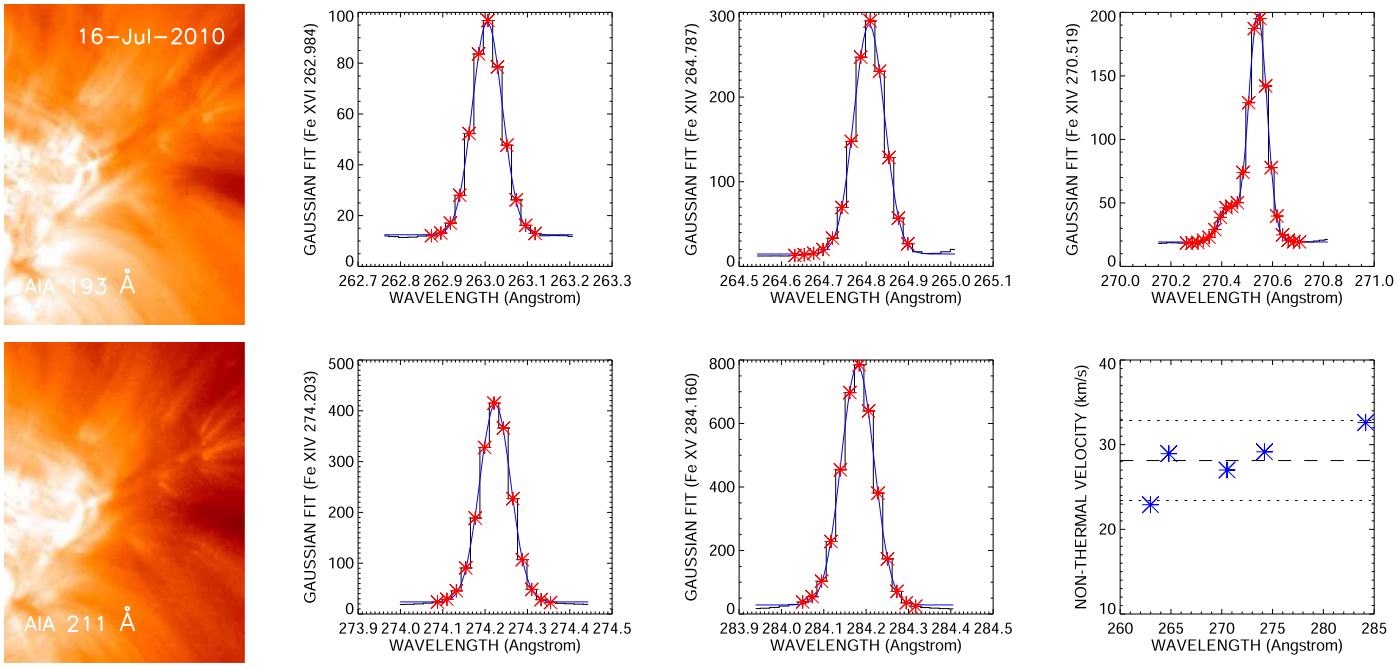

Figure A8. Same as Figure 1 but for the active region NOAA 11087 observed on 2010 July 16.

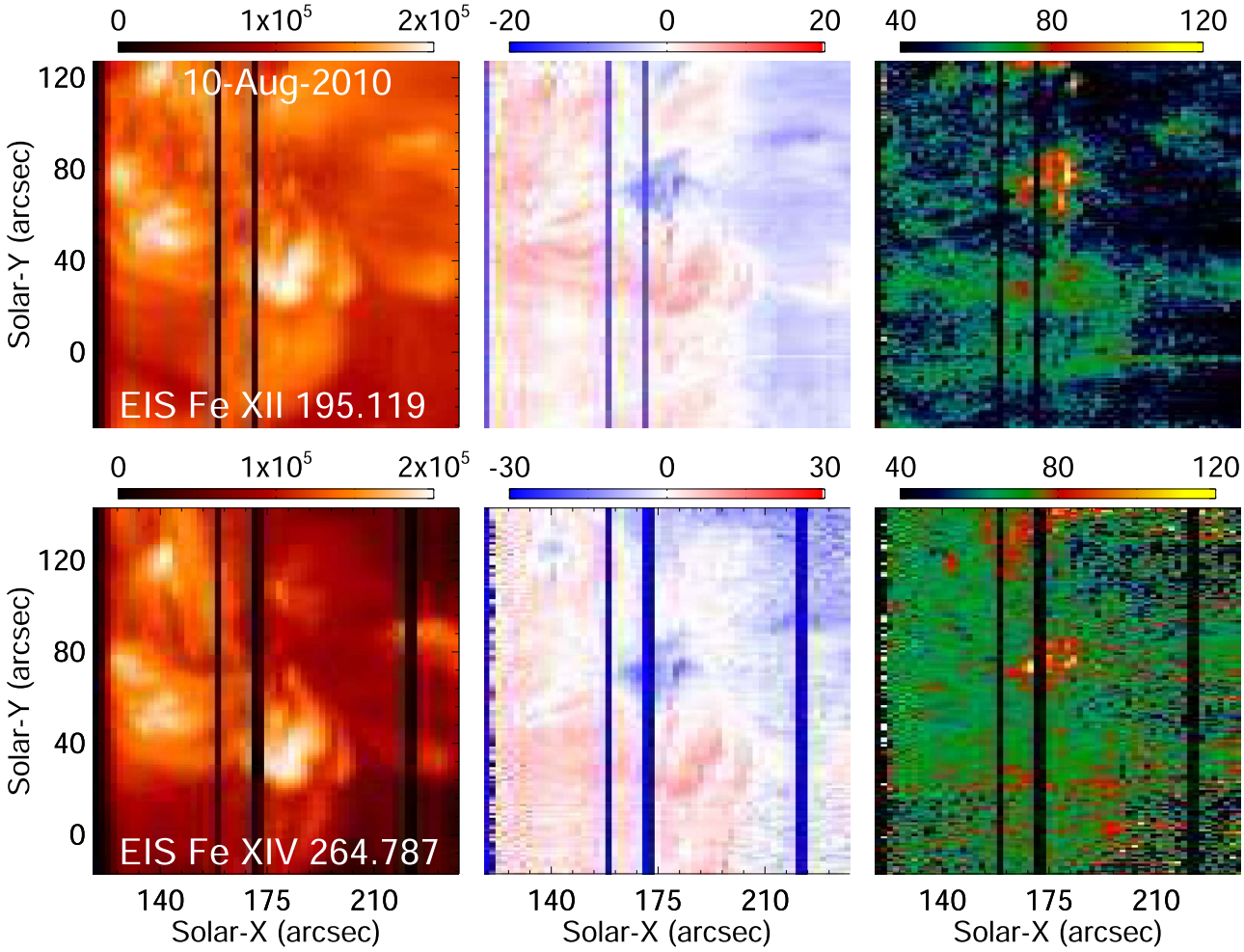

Figure A9. Same as Figure 2 but for the active region NOAA 11093 observed on 2010 August 10.

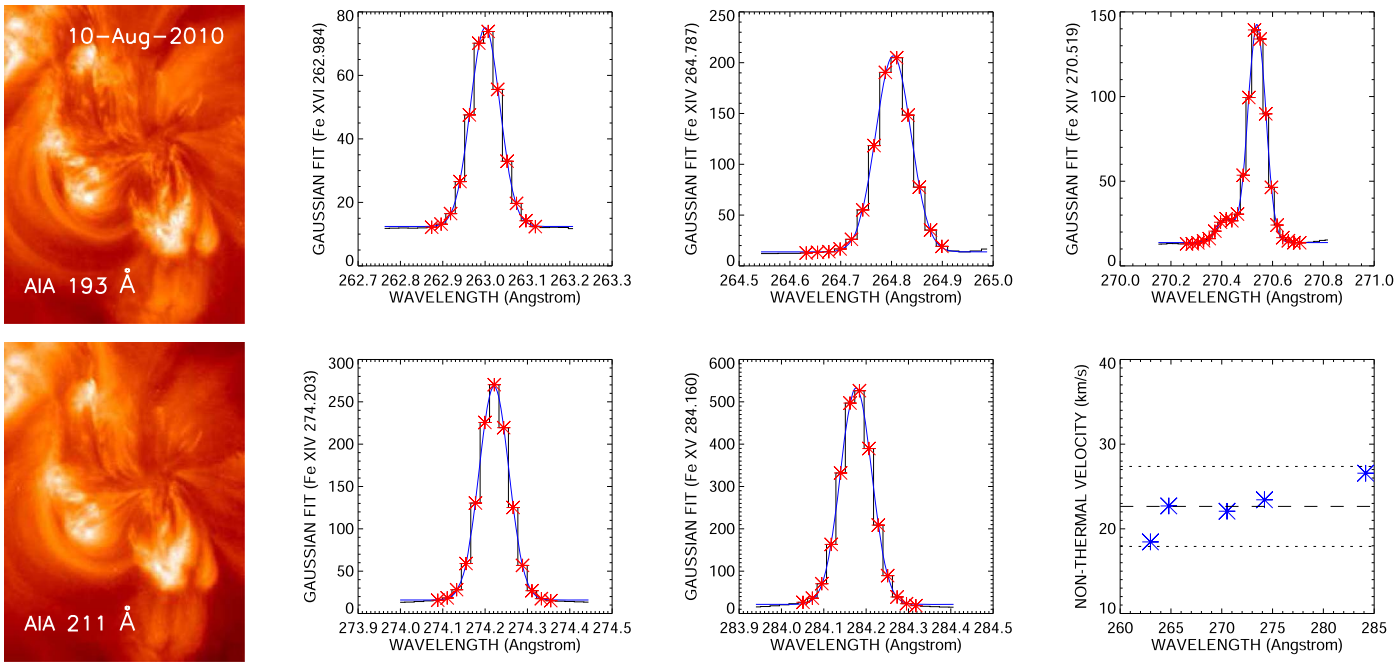

Figure A10. Same as Figure 1 but for the active region NOAA 11093 observed on 2010 August 10.

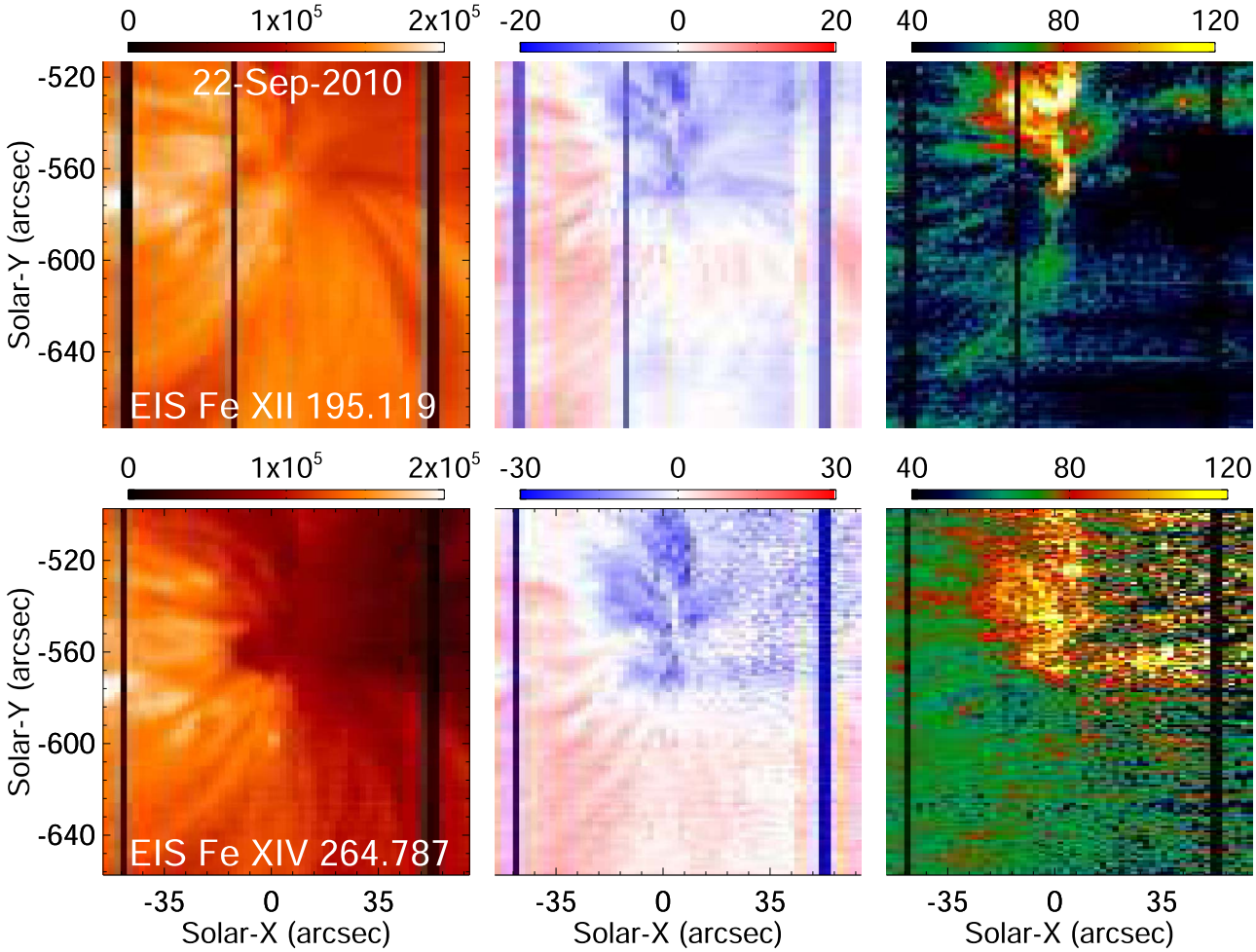

Figure A11. Same as Figure 2 but for the active region NOAA 11108 observed on 2010 September 22.

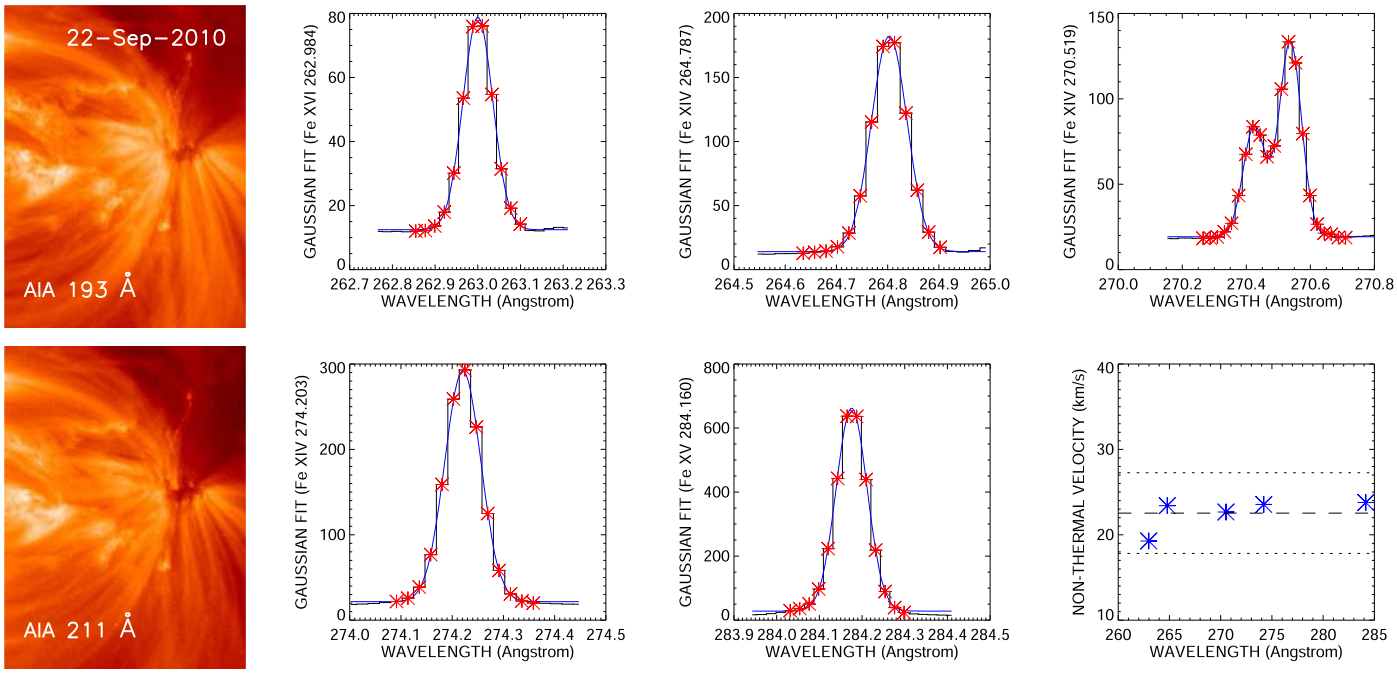

Figure A12. Same as Figure 1 but for the active region NOAA 11108 observed on 2010 September 22.

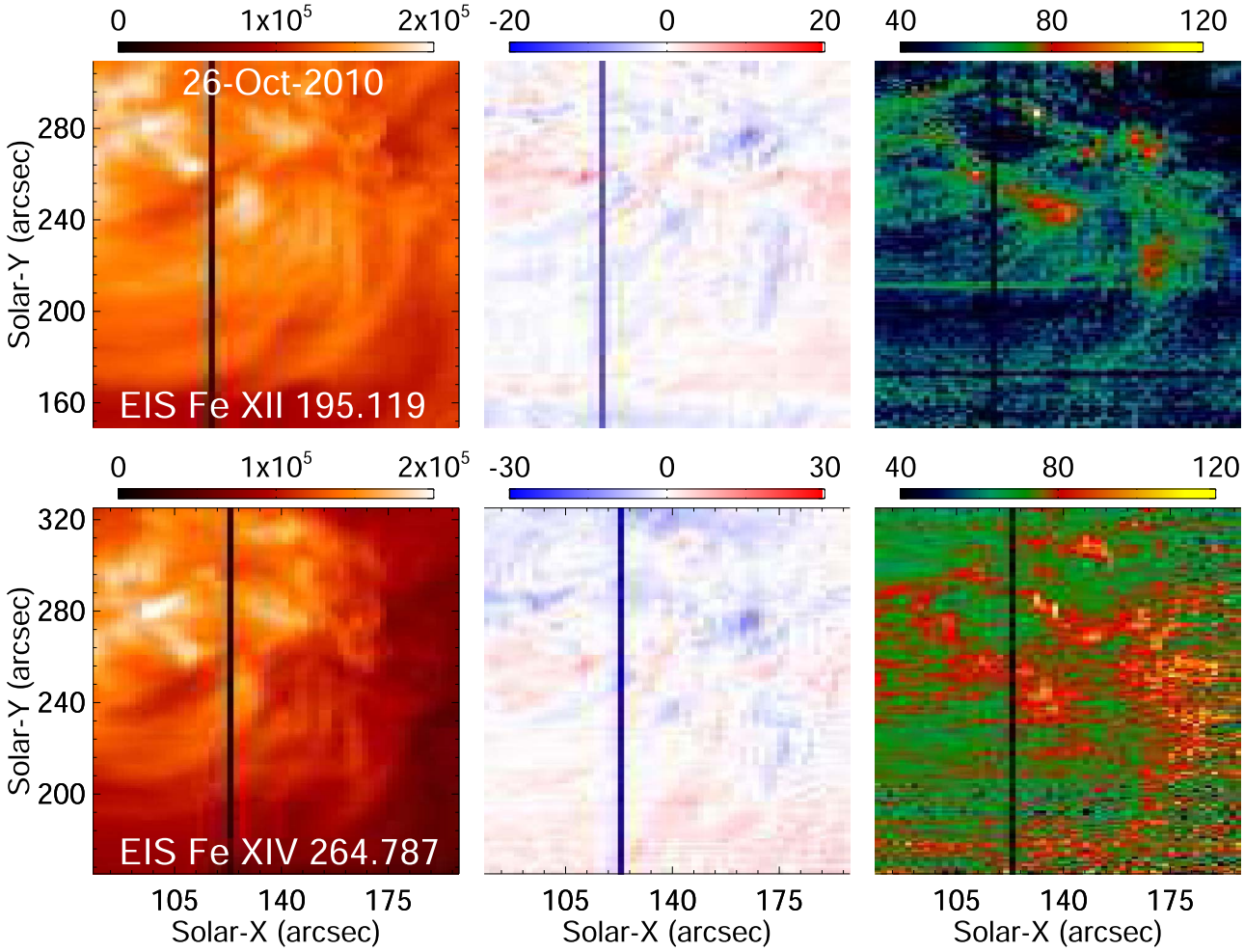

Figure A13. Same as Figure 2 but for the active region NOAA 11117 observed on 2010 October 26.

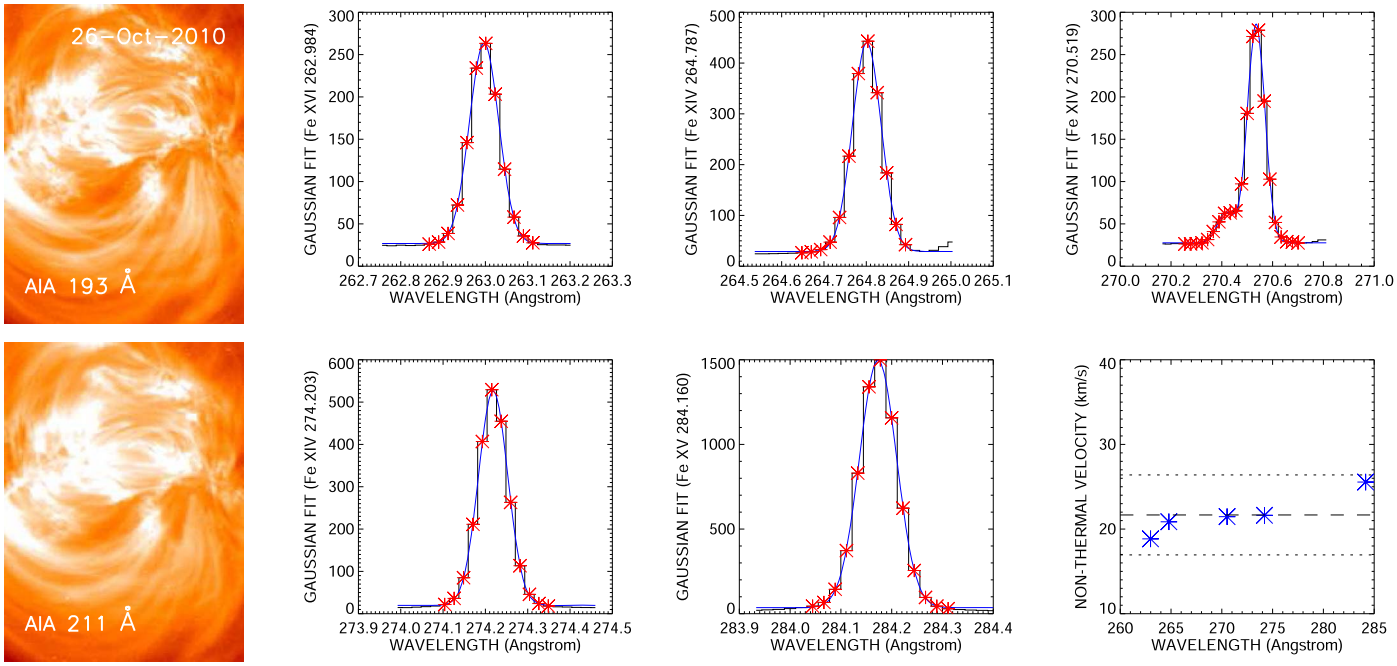

Figure A14. Same as Figure 1 but for the active region NOAA 11117 observed on 2010 October 26.

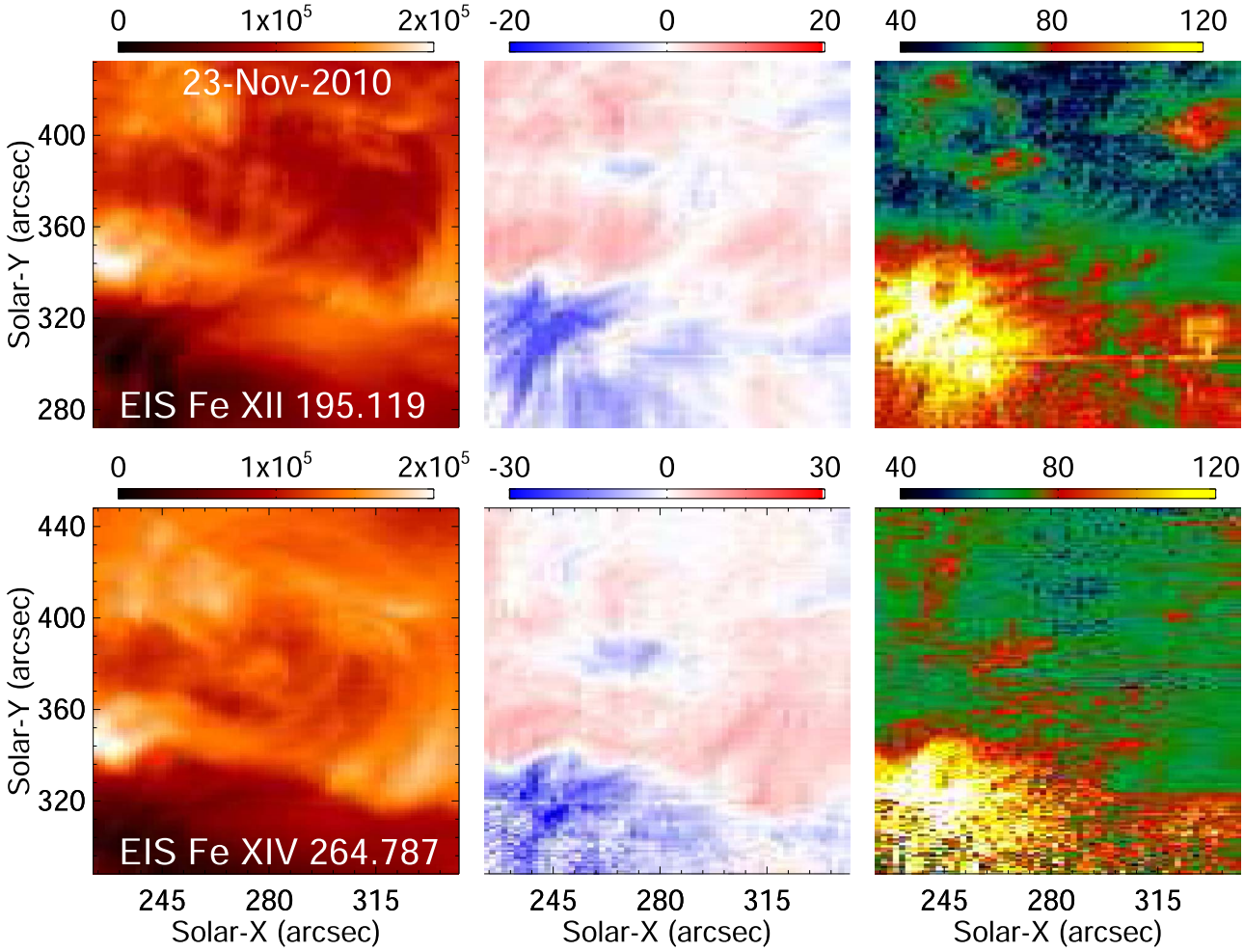

Figure A15. Same as Figure 2 but for the active region NOAA 11127 observed on 2010 November 23.

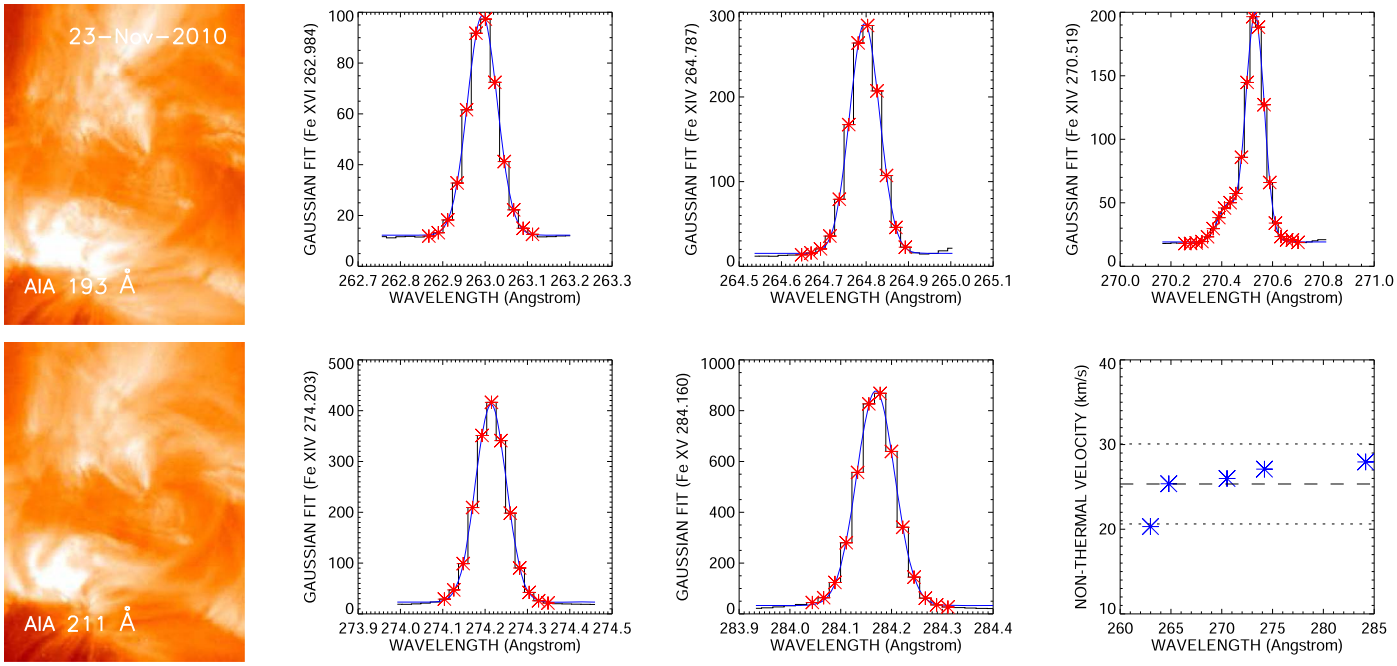

Figure A16. Same as Figure 1 but for the active region NOAA 11127 observed on 2010 November 23.

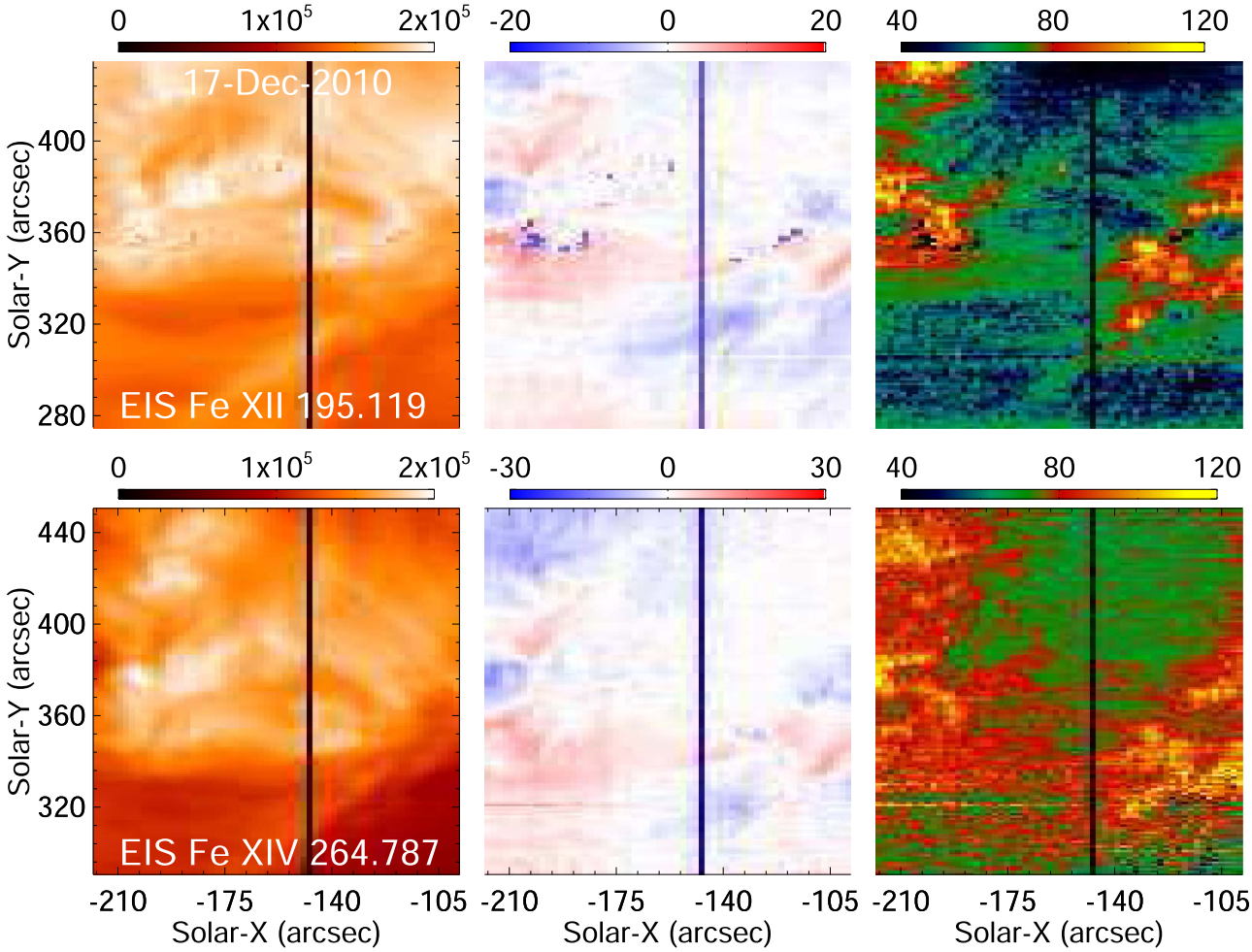

Figure A17. Same as Figure 2 but for the active region NOAA 11135 observed on 2010 December 17.

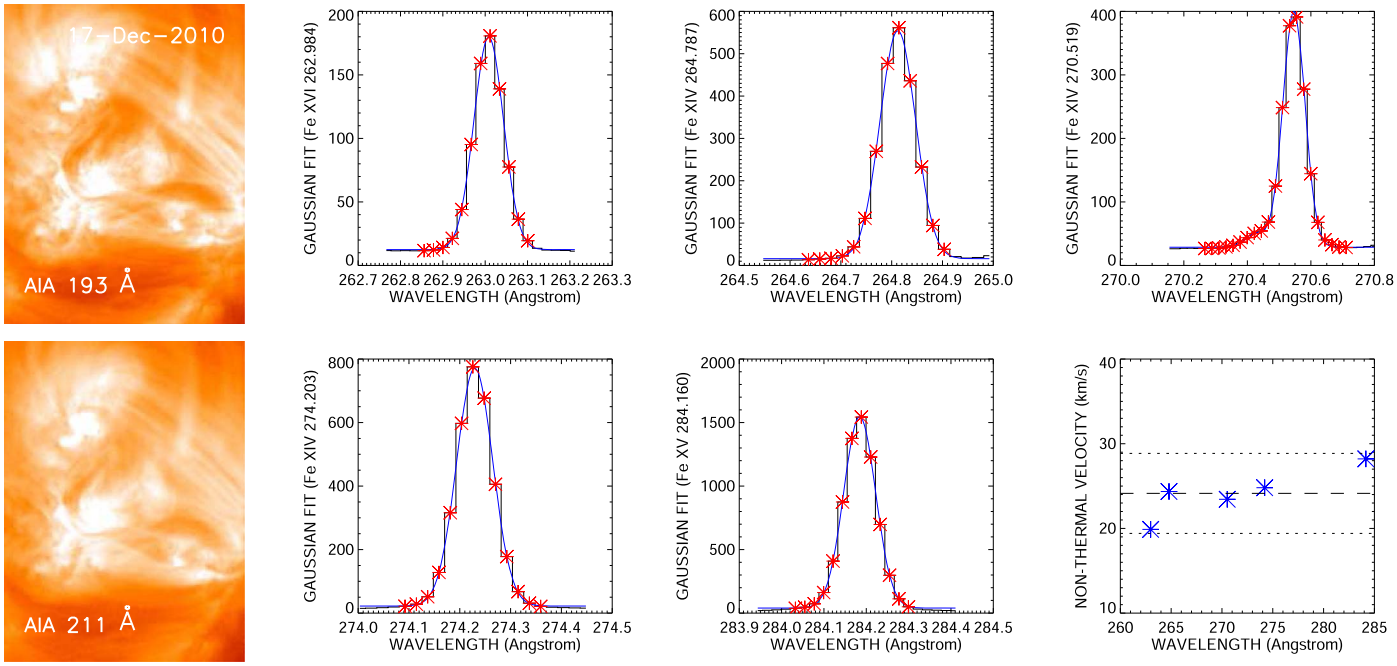

Figure A18. Same as Figure 1 but for the active region NOAA 11135 observed on 2010 December 17.

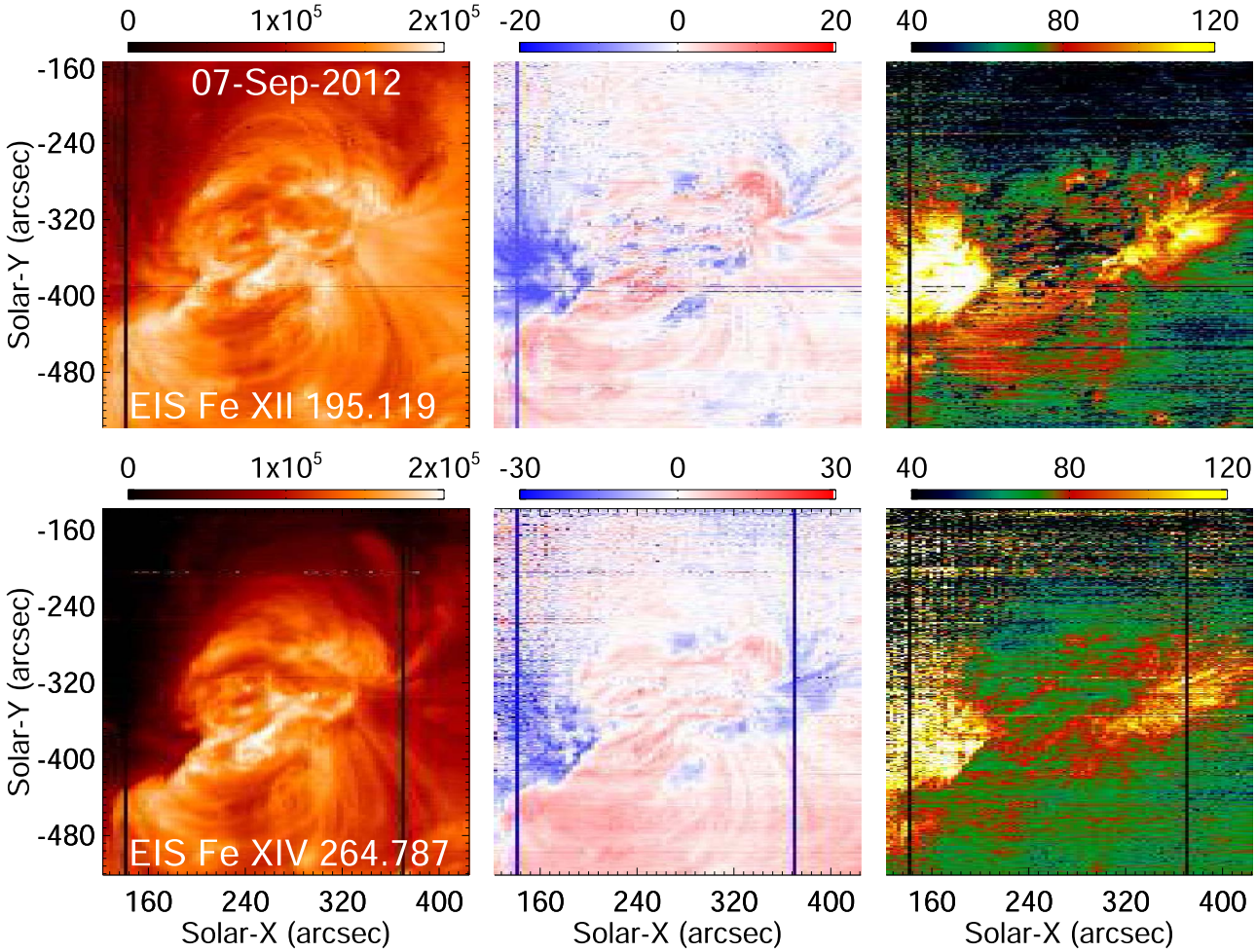

Figure A19. Same as Figure 2 but for the active region NOAA 11564 observed on 2012 September 7.

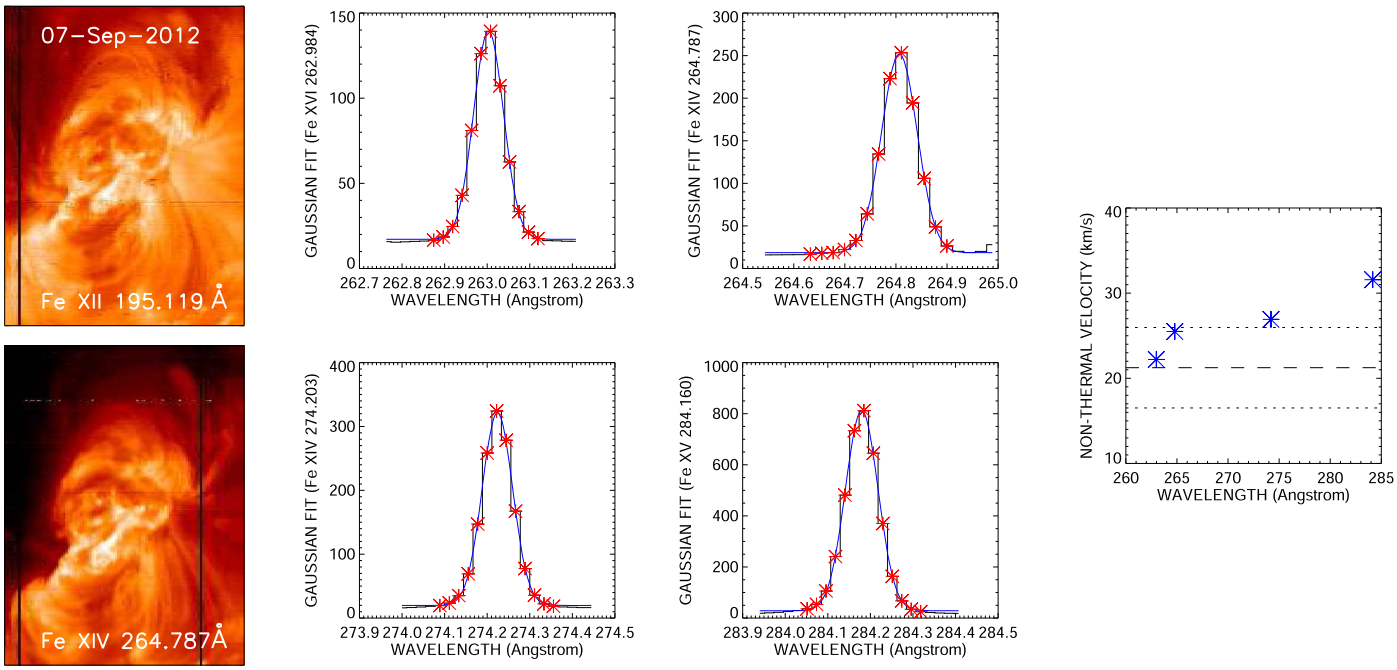

Figure A20. Same as Figure 1 but for the active region NOAA 11564 observed on 2012 September 7.

ORCID iDs

M. Asgari-Targhi https://orcid.org/0000-0003-0204-8385
D. H. Brooks https://orcid.org/0000-0002-2189-9313
M. Hahn https://orcid.org/0000-0001-7748-4179
D. W. Savin https://orcid.org/0000-0002-1111-6610

References

Abramenko, V. I., Carbone, V., Yurchyshyn, V., et al. 2011, ApJ, 743, 133
Acton, L. W., Wolfson, C. J., Joki, E. G., et al. 1981, ApJL, 244, L137
Alfvén, H. 1947, MNRAS, 107, 211
Antolin, P., & Shibata, K. 2010, ApJ, 712, 494
Asgari-Targhi, M., & van Ballegooijen, A. A. 2012, ApJ, 746, 81
Asgari-Targhi, M., van Ballegooijen, & Imada, S. 2014, ApJ, 786, 28
Asgari-Targhi, M., van Ballegooijen, A. A., Cranmer, S. R., & DeLuca, E. E. 2013, ApJ, 773, 111
Billings, D. E., & Lehman, R. C. 1962, ApJ, 136, 258
Brooks, D. H., & Warren, H. P. 2016, ApJ, 820, 63
Brooks, D. H., Warren, H. P., Ugarte-Urra, I., & Winebarger, A. R. 2013, ApJL, 772, 19
Brown, C. M., Feldman, U., Seely, J. F., Korendyke, C. M., & Hara, H. 2008, ApJS, 176, 511
Cargill, P. J., & Klimchuk, J. A. 2004, ApJ, 605, 911
Chitta, L. P., van Ballegooijen, A. A., Rouppe van der Voort, L., DeLuca, E. E., & Kariyappa, R. 2012, ApJ, 752, 48
Coleman, P. J., Jr. 1968, ApJ, 153, 371
Culhane, J. L., Harra, L. K., James, A. M., Al-Janabi, K., Bradley, L. J., et al. 2007, SoPh, 243, 19
De Pontieu, B., Testa, P., Martinez-Sykora, J., Antolin, P., Karampelas, K., et al. 2022, ApJ, 926, 52
De Pontieu, B., Title, A. M., Lemen, J. R., et al. 2014, SoPh, 289, 2733
Doschek, G. A. 2012, ApJ, 754, 153
Doschek, G. A., & Feldman, U. 1977, ApJL, 212, L143
Doschek, G. A., Mariska, J. T., Warren, H. P., Brown, C. M., Culhane, J. L., et al. 2007, ApJL, 667, L109
Elsasser, W. M. 1950, PhRv, 79, 183
Hahn, M., Asgari-Targhi, M., & Savin, D. W. 2023, ApJ, 953, 3
Hara, H., & Ichimoto, K. 1999, ApJ, 513, 969
Heyvaerts, J., & Priest, E. R. 1983, A&A, 117, 220
Hollweg, J. V., Jackson, S., & Galloway, D. 1982, SoPh, 75, 35
Ichimoto, K., Hara, H., Takeda, A., Kumagai, K., Sakurai, T., et al. 1995, ApJ, 445, 978
Imada, S., Hara, H., & Watanabe, T. 2009, ApJL, 705, L208
Imada, S., Hara, H., Watanabe, T., et al. 2008, ApJL, 679, L155
Imada, S., & Zweibel, E. G. 2012, ApJ, 755, 93
Ionson, J. A. 1985, SoPh, 100, 289
Kamio, S., Hara, H., Watanabe, T., Fredvik, T., & Hansteen, V. H. 2010, SoPh, 266, 209
Knight, J. W., Newman, C. E., & Sturrock, P. A. 1974, SoPh, 37, 183
Korendyke, C. M., Brown, C. M., Thomas, R. J., Keyser, C., Davila, J., et al. 2006, ApOpt, 45, 8674
Lemen, J. R., Title, A. M., Akin, D. J., Boerner, P. F., Chou, C., et al. 2012, SoPh, 275, 17
Mandrini, C. H., Démoulin, P., & Klimchuk, J. A. 2000, ApJ, 530, 999
Mariska, J. T., & Muglach, K. 2010, ApJ, 713, 573
Matsumoto, T., & Shibata, K. 2010, ApJ, 710, 1857
McIntosh, S. W., De Pontieu, B., Carlsson, M., Hansteen, V., Boerner, P., et al. 2011, Natur, 475, 477
Milano, L. J., Gómez, D. O., & Martens, P. C. H. 1997, ApJ, 490, 442E
Parker, E. N. 1972, ApJ, 174, 499
Parker, E. N. 1983, ApJ, 264, 642
Parker, E. N. 1988, ApJ, 330, 474
Patsourakos, S., & Klimchuk, J. A. 2006, ApJ, 647, 1452
Patsourakos, S., & Klimchuk, J. A. 2009, ApJ, 696, 760
Strauss, H. R. 1976, PhFl, 19, 134
Strauss, H. R. 1997, JPlPh, 57, 83
Testa, P., De Pontieu, B., & Hansteen, V. 2016, ApJ, 827, 99
Tian, H., McIntosh, S. W., De Pontieu, B., Martínez-Sykora, J., Sechler, M., et al. 2011, ApJ, 738, 18
Tripathi, D., Klimchuk, J. A., & Mason, H. E. 2011, ApJ, 740, 111
Tripathi, D., Mason, H. E., Dwivedi, B. N., Del Zanna, G., & Young, P. R. 2009, ApJ, 694, 1256
Uchida, Y., & Kaburaki, O. 1974, SoPh, 35, 451
van Ballegooijen, A. A., & Asgari-Targhi, M. 2018, JPhCS, 1100, 012027
van Ballegooijen, A. A., Asgari-Targhi, M., & Berger, M. A. 2014, ApJ, 787, 87
van Ballegooijen, A. A., Asgari-Targhi, M., Cranmer, S. R., & DeLuca, E. E. 2011, ApJ, 736, 3
van Ballegooijen, A. A., Asgari-Targhi, M., & Voss, A. 2017, ApJ, 849, 46
Warren, H. P., Brooks, D. H., & Winebarger, A. R. 2011, ApJ, 734, 90
Wentzel, D. G. 1974, SoPh, 39, 129
Young, P. R. 2011, EIS Software Note no. 7, Solar Software, SSW/hinode/eis/doc/eisnotes, https://hesperia.gsfc.nasa.gov/ssw/hinode/eis/doc/eis_notes/07_LINE_WIDTH/eis_swnote_07.pdf
Young, P. R., Del Zanna, G., Mason, H. E., et al. 2007, PASJ, 59, S857